

1  
2  
3  
4  
5  
6  
7  
8  
9  
10  
11  
12  
13  
14  
15  
16  
17  
18  
19  
20  
21  
22  
23  
24  
25  
26  
27  
28  
29

## Supplementary Information for

### **Tissue-specific geometry and chemistry of modern and fossilized melanosomes reveal internal anatomy of extinct vertebrates**

Valentina Rossi\*, Maria E. McNamara\*, Sam Webb, Shoshuke Ito, Kazumasa Wakamatsu

Valentina Rossi and Maria E. McNamara

Email: [valentina.rossi@ucc.ie](mailto:valentina.rossi@ucc.ie); [maria.mcnamara@ucc.ie](mailto:maria.mcnamara@ucc.ie)

#### **This PDF file includes:**

- Supplementary Text
- Supplementary Methods
- Figs. S1 to S29
- Captions for Datasets S1 to S16
- References for SI Text and Datasets

## 30 **Supplementary Text**

31

32 **Impact of the enzymatic extraction on melanosomes.** Enzymatic melanin extraction  
33 (EME) has been used previously to isolate melanosomes from integumentary (1, 2) and non-  
34 integumentary tissues (3) in order to analyze melanosome morphology, organic chemistry  
35 and metal content (1–4). Previous studies have, however, reported a bias in the EME  
36 procedure towards recovery of eumelanosomes (1).

37

38 In this study, the melanin extracts from amphibian and reptile tissues are typically dark  
39 brown to black, but extracts for birds and mammals are usually orange (except for the eyes  
40 and hair, which, usually yield dark-colored extracts). As in the feathers, dark-colored extracts  
41 from all tissues and taxa contain abundant, fully three-dimensional melanosomes with a  
42 regular smooth surface and little to no associated amorphous matter; orange extracts contain  
43 abundant amorphous organic matter in addition to melanosomes. The latter include rare  
44 fractured melanosomes with an internal void; this hollow structure is interpreted as EME-  
45 induced damage. Melanin extracts with damaged melanosomes contain melanin (as  
46 evidenced by AHPO analyses) and were used for analyses of inorganic chemistry but not of  
47 melanosome geometry. In reptiles, the majority (61%;  $n = 70$ ) of extracts contain pristine  
48 melanosomes; 42% of amphibian extracts contain pristine melanosomes ( $n = 63$ ). In contrast,  
49 only 11% ( $n = 63$ ) of avian extracts and 32% ( $n = 56$ ) of mammalian extracts contain pristine  
50 melanosomes.

51

52 These data suggest that pheomelanin concentrations may be under-reported in our AHPO  
53 analyses; this limitation of the technique should apply equally to all samples analyzed and  
54 thus comparison of the relative abundance of eu- and phaeomelanin among samples is still  
55 valid.

56

57 **Geometry of melanosomes.** The geometry of melanosomes varies both within and among  
58 taxa. For some taxa, e.g., the African clawed frog (*X. laevis*, Fig. S6A), the fire-bellied newt  
59 (*C. orientalis*, Fig. S6E) and the leopard gecko (*E. macularius*, Fig. S6F), scatterplots of  
60 melanosome geometry show extensive overlap of morphospace regions for different tissues.  
61 In other taxa, melanosomes from certain tissues plot separately. In the brown basilisk (*B.*  
62 *basiliscus*, Fig. S6B), melanosomes from the skin, liver and spleen are similar in size and  
63 smaller than those from connective tissue and the eyes. In the green anole (*A. carolinensis*,  
64 Fig. S6G), eye melanosomes are consistently larger than those from all other organs. The  
65 black iguana (*C. similis*, Fig. S6C) shows a similar trend, excepting the spleen melanosomes,  
66 which are more variable in size than in the anole. In the brown mouse (*M. musculus*, Fig.  
67 S6D), melanosomes from the skin, hair and kidney are larger than those from the liver and  
68 spleen. In the zebra finch (*T. guttata*, Fig. S6H) there is substantial overlap between  
69 morphospace regions occupied by melanosomes from the skin, heart and eyes. Differences in  
70 melanosome geometry among tissues are more readily visualized using box plots of the  
71 length, width and aspect ratio of the melanosomes (Figs. S7-S14). For each of these  
72 variables, the box plots reveal which tissues in each taxon contain melanosomes that differ  
73 strongly from those of another tissue or tissues. The data for each taxon shows at least tissue  
74 for which the range of standard deviation of melanosome length, width or aspect ratio does  
75 not overlap with the data for at least one other tissue. ANOVA test results confirm that  
76 differences in melanosome geometry among tissues within individual taxa are statistically  
77 significant. These differences in geometry are represented schematically in Figs. S7B–S14B  
78 and Figs. S16B–S19B.

79

80 **Geometry of fossil melanosomes.** In the fossil tadpole NHML4999 (*P. pueyoi*, Fig. S16)  
81 melanosomes from the skin and internal organs have similar aspect ratios. Melanosomes from  
82 longest to shortest are those from the lungs (sample 6), tail (samples 4 and 5; corresponding  
83 to collagenous fascia, myomeres and nerve cord), skin (sample 3), and liver (sample 2). In the  
84 fossil frog NHML4982 (*P. pueyoi*, Fig. S17) melanosomes from the skin and internal organs  
85 have similar aspect ratios, with the exception of those from the liver (sample 2) which are  
86 slightly slenderer Melanosomes from longest to shortest are those from the thorax (sample 8,  
87 possibly derived from the lungs), skin (sample 9a), and (possibly) the liver (sample 9b).  
88 Tissue-specific patterns of fossil melanosome geometry therefore resemble those of modern  
89 amphibians, where non-integumentary melanosomes from lungs and connective tissues are  
90 larger than those from the integument and the liver. The fossil reptile HNMD-Me9018  
91 (Reptilia indet., Fig. S18) shows two distinct layers of melanosomes only in sample 11, with  
92 similar morphologies. In the fossil bat HNMD-Me7069b (Chiroptera indet., Fig. S19)  
93 melanosomes from the integument and internal organs have similar aspect ratios, with the  
94 exception of the melanosomes from one region of the skin (sample 13). Melanosomes from  
95 the internal organs (samples 14 and 15) are larger than those from the skin (samples 13 and  
96 16). This result differs to patterns of melanosome geometry in the extant brown mouse (*M.*  
97 *musculus*, Fig. S14), where integumentary melanosomes are larger than non-integumentary  
98 melanosomes. This difference might reflect interspecific differences across different  
99 mammalian taxa.

100

## 101 **Supplementary Methods**

102

103 **Enzymatic melanin extraction (EME).** Tissue samples were washed with acetone (1 x 1  
104 ml) and biomolecular grade water (3 x 1 ml). Samples were added to a solution of 1.5 ml  
105 phosphate buffer (PB) and 15 µl of DTT (solution 1), incubated for 24 h at 37.5°C and stirred  
106 at 200 rpm. Samples were dissected, immersed in a solution of 1.5 ml PB, 15 µl DTT and 5  
107 mg of Proteinase-K (solution 2) and incubated as in the previous step. Samples were then  
108 centrifuged for 4 min at 5500 rpm, placed in a solution of 1.5 PB, 15µl DTT and 5 mg of  
109 Papain (solution 3) and incubated as above. Centrifuged samples were washed with  
110 biomolecular grade water (3 x 1 ml), added to solution 1 and incubated for 24 h as above.  
111 Triton X-100 (0.05 ml/1 ml) was added and samples stirred at 200 rpm for 4 h at 37°C.  
112 Samples were then washed with biomolecular-grade water (5 x 1 ml), added to solution 1 and  
113 incubated for 24 h. Next, samples were washed with acetone (1 x 1 ml) and with  
114 biomolecular-grade water (3 x 1 ml). Solution 1 was added and the samples incubated as  
115 above. This final series of steps (washing with acetone, addition to solution 1 and incubation)  
116 was repeated three times. Finally, samples were washed with biomolecular-grade water (4–6  
117 x 1 ml) and dried for three days. This protocol includes fewer washing steps than the original  
118 protocol (1) in order to maximize the amount of melanin recovered.

119

120 Extracts were screened using SEM and only extracts containing pristine melanosomes (n =  
121 95; Fig. S1–S3, Datasets S1 and S4) were analyzed further. Melanosomes are present in only  
122 one internal tissue in the dwarf African clawed frog (*H. boettgerii*), Java sparrow (*L.*  
123 *oryzivora*), woodcock (*S. rusticola*), domestic sheep (*O. aries*) and domestic pig (*S. scrofa*);  
124 these taxa are not considered further here as the data are not amenable to intra-taxon  
125 comparative analysis.

126

127 **Histology.** Following wax embedding and sectioning, sections were deparaffinized by  
128 immersion in xylene (2 x 2 min), 50:50 xylene:ethanol (2 min), 100% EtOH (2 min), 90%  
129 EtOH (2 min), 70% EtOH (2 min), 50% EtOH (2 min), 30% EtOH 2 (min), tap water (5 sec)

130 and distilled water (5 sec). Tissues were fixed for 5 min in acetone and rinsed in acidulated  
131 water. Sections were then immersed in a solution of 2% silver nitrate, 5% gelatin and 0.15%  
132 hydroquinone for 15 seconds to stain only melanin (staining for >2 min can result in staining  
133 of non-melanin tissue components). Sections were then rinsed successively in hot water  
134 (55°C) and DD water, immersed for 2 min in 5% sodium thiosulfate and dehydrated with the  
135 inverse procedure described above and coverslipped.

136

137 **Geometry of melanosomes.** Data on melanosome geometry for each tissue in each modern  
138 taxon and fossil specimen were tested for normality and homoscedasticity. Differences in  
139 geometry among samples were tested using ANOVA and the post-hoc Tukey HSD test where  
140 the assumptions of normality and homoscedasticity were not violated. Data with non-normal  
141 distributions were log-transformed and analyzed either with the ANOVA and Tukey tests  
142 (where the transformed data were normally distributed) or the non-parametric Kruskal-Wallis  
143 and Mann-Whitney tests (where the transformed data were not normally distributed). In the  
144 case of only two samples the t-test was used.

145

146 **Linear Discriminant Analysis of metal chemistry.** The metal chemistry of melanosomes  
147 was analyzed using Linear Discriminant Analysis (LDA, also known as discriminant function  
148 analysis). LDA attempts to model differences among pre-defined groups, by maximizing the  
149 separation among those groups. The output of the analysis is a scatterplot that shows selected  
150 linear discriminants (LDs) on the x and y axis. The test also produces a biplot that shows the  
151 contribution of each variable to the variation in the scatterplot; these data are a schematic  
152 representation of the LDA loadings. In the biplot, each variable is represented as an arrow,  
153 the length of which is determined by the loadings; longer arrows indicate variables that  
154 contribute more to the variation in the dataset. The direction of the arrows indicates the  
155 orientation of the axis along which the values for that variable increase. Our LDA results  
156 produce good separation among groups, with the sum of LD1 and LD2 accounting for 88% –  
157 100% of the variance in the data for different taxa.

158

159 **Synchrotron X-ray Fluorescence.** The fossil soft tissue samples and the melanin extracts  
160 are complex heterogeneous materials. This renders quantification difficult. We used units of  
161 concentration based on an area basis ( $\mu\text{g}/\text{cm}^2$ ) rather than volume basis as it is challenging to  
162 make accurate matrix and depth corrections for complex heterogeneous materials. While such  
163 corrections certainly can be made, we feel that it would be an additional source of error and  
164 uncertainty in the reporting of the results. Our samples may also vary slightly in thickness; it  
165 is not possible, however, to quantify this variation over entire fossils at micron-scale  
166 resolution. Previous studies have indicated that XRF maps are not sensitive to spatial  
167 variations in samples that vary from 50-100  $\mu\text{m}$  thick (5). Many of our samples fall within  
168 this thickness range and thus lateral spatial variations in sample thickness are unlikely to  
169 impact elemental concentrations calculated from XRF maps. In the fossil bat Me7069b  
170 (Chiroptera indet., Fig. 5C, D and Fig. S21) similar chemical signal across different elements,  
171 on the top right of the maps, is an artefact of the topography of the host rock and it is not  
172 considered in any of the interpretation of the metal chemistry.

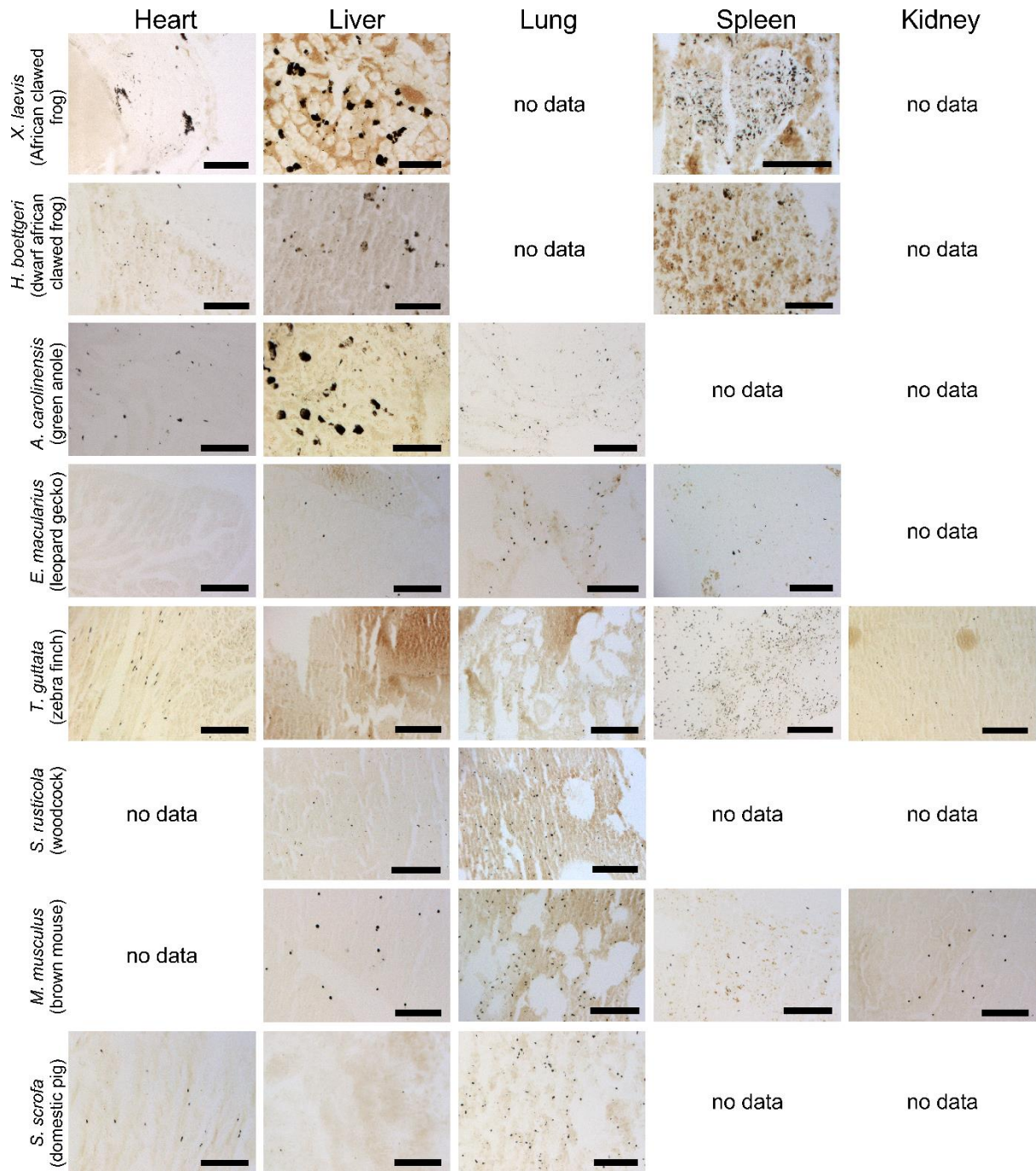
173 **Quantification.** Calculation of element concentrations was performed using NIST traceable  
174 thin film analytical standards; this is accurate to a given area based on the overall beam line  
175 parameters at the time of data collection and with a given setup. The counts collected over a  
176 region of interest (ROI) of the thin film standard were then normalized to the I0 intensity to  
177 calibrate the fluorescence counts to a concentration in  $\mu\text{g}/\text{cm}^2$ . Final maps were screened  
178 post-acquisition to avoid overinterpretation of the distribution and concentration of elements.

179  
180  
181  
182  
183  
184  
185  
186  
187  
188  
189  
190  
191  
192  
193  
194  
195  
196  
197  
198

**Peak interpretation.** XRF spectra were produced for several regions of interest (Figs. S23–S28) in representative modern samples, and all fossil samples, using the MCA spectra function in SMAK. The MCA spectra show well-constrained peaks for each of Ca, Ti (only in fossil samples), Fe, Cu, and Zn that do not overlap with key peaks for other elements mapped. All peaks were fitted using SMAK parameters configuration (Spectrometer Zero, Spectrometer Gain, and Detector Width) that will find the best fit of the spectrum of interest. Other elements that show low concentrations and/or are not associated with any melanosomes rich regions were not analyzed further in this work. Further deconvolutions of the peaks were not required for other elements and melanosomes samples. In the fossil tadpole NHML4999 (*P. pueyoi*, Fig. 4, Figs. S21 and S22A), Fe and Mn show similar spatial distributions in XRF maps (Fig. 4 and Figs. S21, S22A, S28). A single peak occurs in the region of the spectrum that typically features both the K-alpha peak for Fe and the K-alpha peak for Mn. In the fitted MCA spectrum for ROI5 (Fig. S22A and Fig. S29), there is a very small peak for Mn (Fig. S29A–C). Scatterplots of Fe *versus* Mn for the fossil tadpole reveal two distinct distributions for the two elements, with little overlap (Fig. S29D). Importantly, Fe is present in high concentrations in fitted maps for ROI5 (Fig. S29E); in contrast, Mn is very low in concentration in spectra for ROI5, but is enriched in fitted maps for the posterior of the eye spot and in the tail (Fig. S29F). ROI5 is interpreted as rich in Fe and not Mn.

199  
200  
201  
202  
203  
204  
205  
206

**ANOVA of metal chemistry for fossil specimens.** We analyzed variation in the concentrations of six elements (Fe, Ca, Cu, Zn, K, Ti) in our melanin extracts and fossil samples using our SRS-XRF data. We selected these elements for the following reasons: 1) they have the highest LDA loadings for all fossil taxa; 2) modern melanin is known to have a high affinity for Fe, Ca, Zn and Cu; 3) Ti concentrations are high and localized in the fossils; 4) K is associated with the sediment.



207

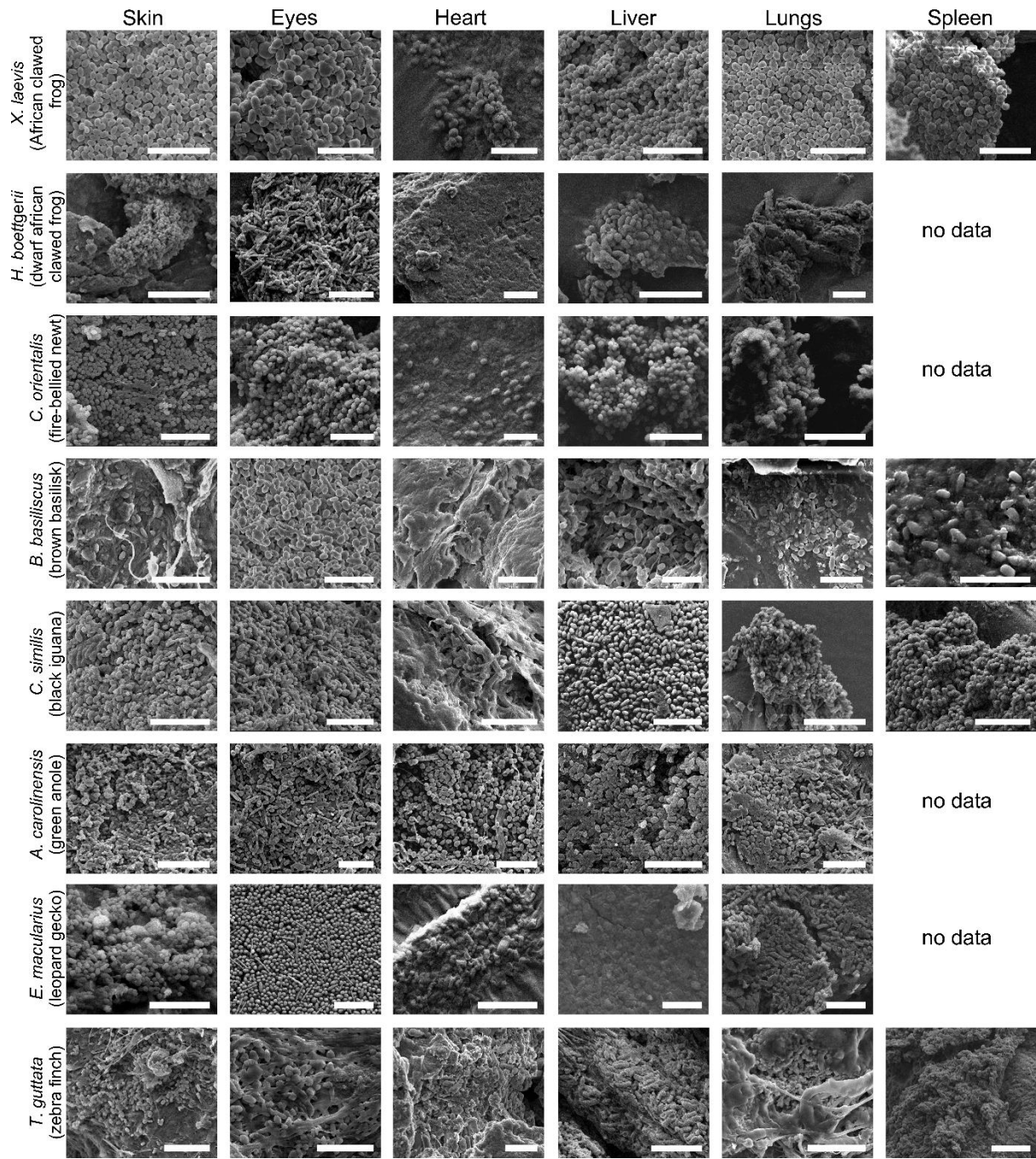
208 **Fig. S1.** Histological sections of modern tissues. Tissue sections are stained using the  
 209 Warthin-Starry procedure. Melanosome aggregates appear black. 'No data' indicates tissues  
 210 for which sectioning was not possible or unsuccessful. Scale bar: 100  $\mu$ m.

211

212

213



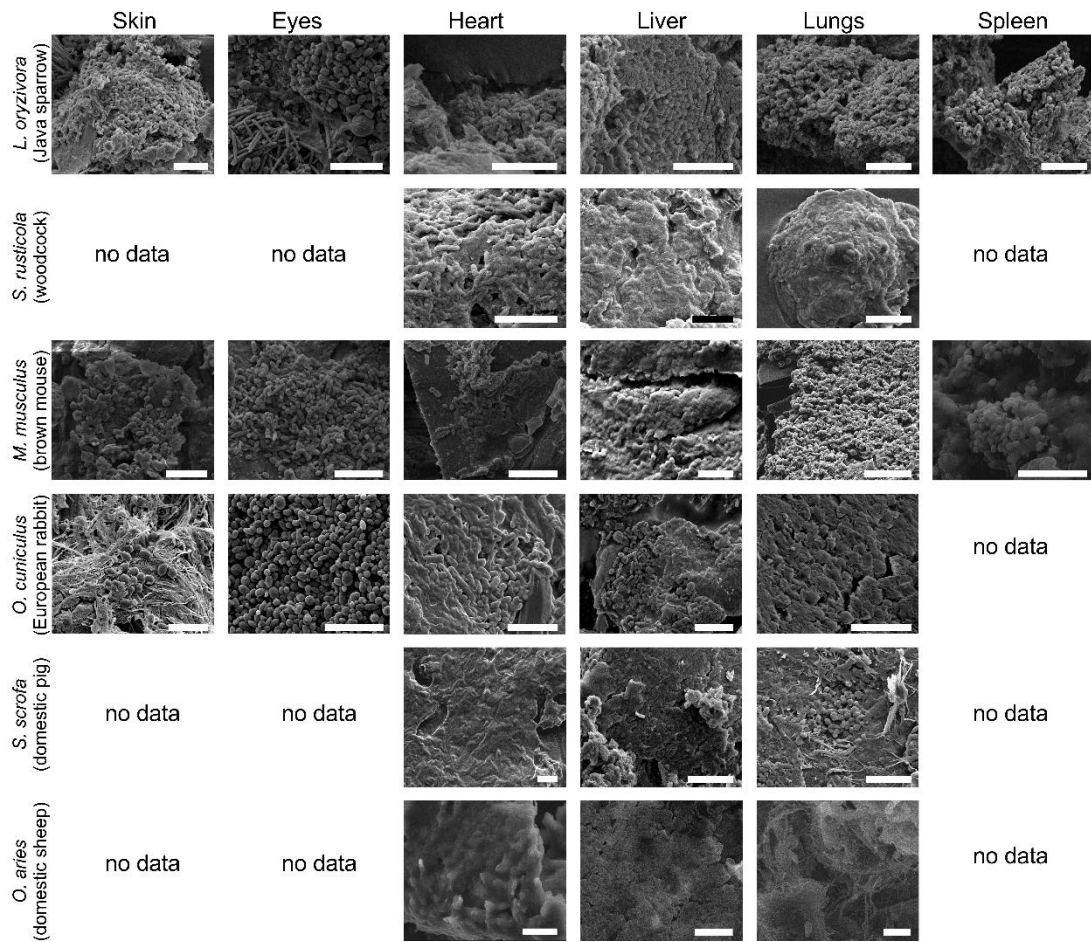


214

215 **Fig. S2.** SEM images of modern melanosomes, in extracts from different taxa and tissues.

216 'No data' indicates tissues that failed to yield extracts. Scale bar: 5  $\mu$ m.

217

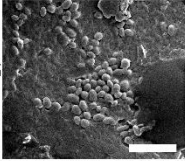
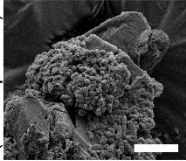
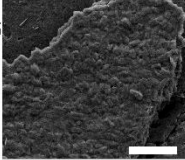

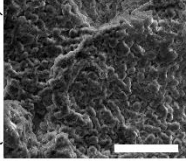
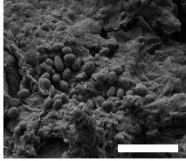
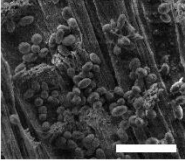
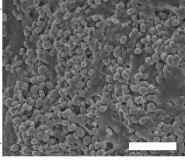
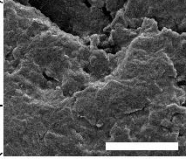
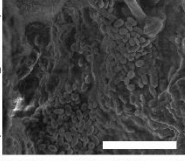
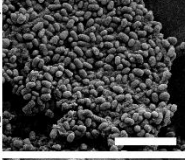
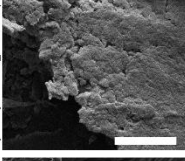
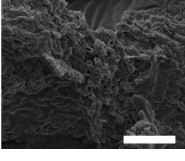
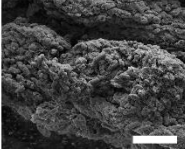


218

219 **Fig. S3.** SEM images of modern melanosomes in extracts from different taxa and tissues. ‘No  
 220 data’ indicates tissues that failed to yield extracts. Scale bar: 5  $\mu$ m.

221



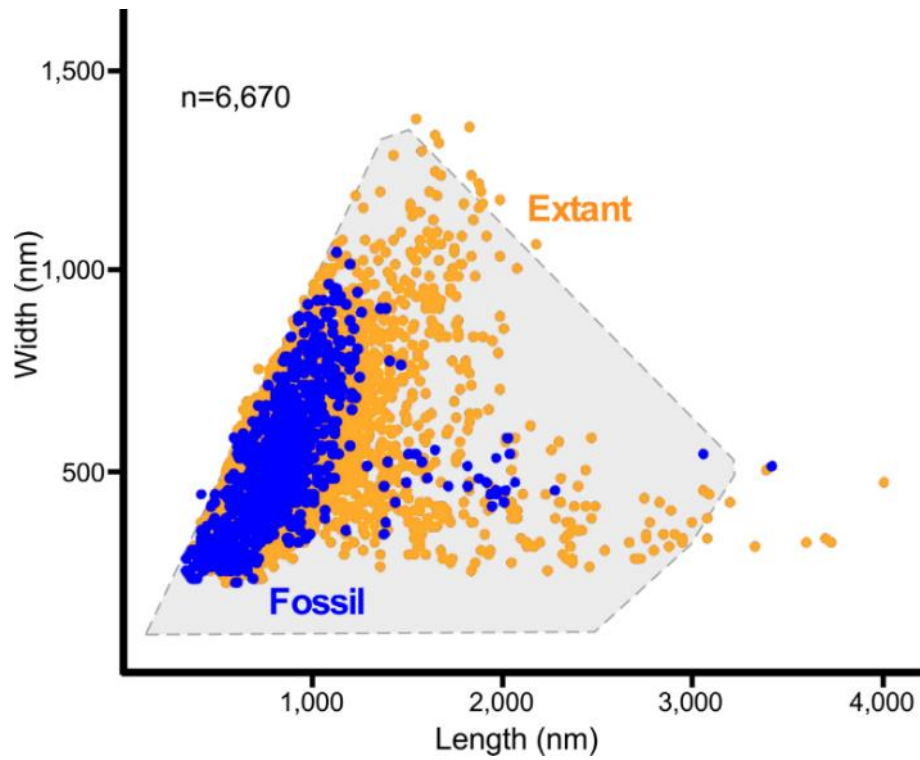
<i>X. laevis</i> (African clawed frog)	C. tissue	Kidney		no data	<i>L. oryzivora</i> (Java sparrow)	C. tissue	Kidney	Hair		no data	no data
<i>H. boettgerii</i> (dwarf african clawed frog)				no data	<i>S. rusticola</i> (Woodcock)					no data	no data
<i>C. orientalis</i> (fire-bellied newt)	no data	no data			<i>M. musculus</i> (brown mouse)						
<i>B. basiliscus</i> (brown basilisk)				no data	<i>O. cuniculus</i> (European rabbit)					no data	no data
<i>C. similis</i> (black iguana)				no data	<i>S. scrofa</i> (domestic pig)					no data	no data
<i>A. carolinensis</i> (green anole)				no data	<i>O. aries</i> (domestic sheep)					no data	no data
<i>E. macularius</i> (leopard gecko)				no data							
<i>T. guttata</i> (zebra finch)											

222

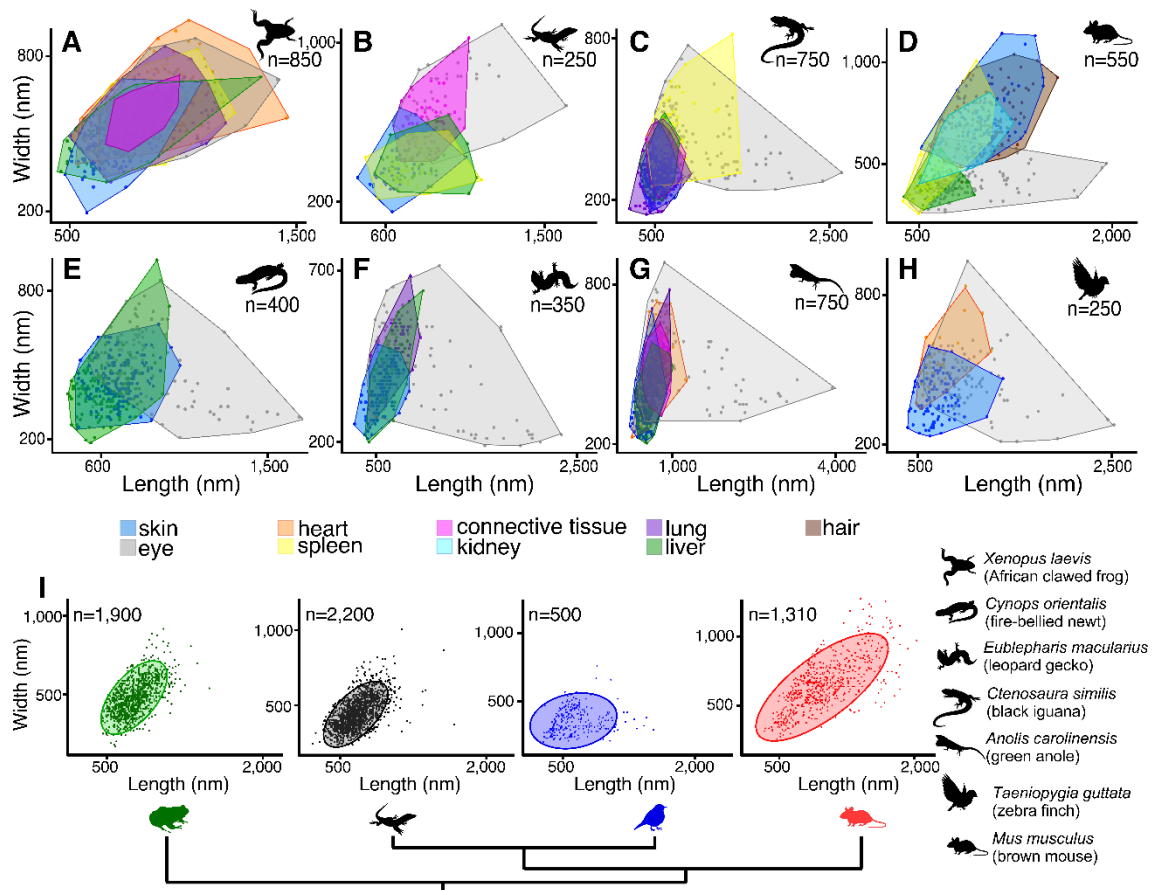
223 **Fig. S4.** SEM images of modern melanosomes in extracts from different taxa and tissues. 'No  
 224 data' indicates tissues that failed to yield extracts. C. tissue refers to connective tissue. Scale  
 225 bar: 5  $\mu$ m.

226

227  
228  
229  
230  
231  
232  
233  
234  
235  
236  
237  
238  
239  
240  
241  
242



**Fig. S5.** Summary plot of melanosome morphospace. The melanosome measurements reported here (blue and orange datapoints for fossil and extant melanosomes, respectively) overlap with those in ref. 25 (main text), which is depicted here as a gray polygon. Our data increase slightly the size of the morphospace.

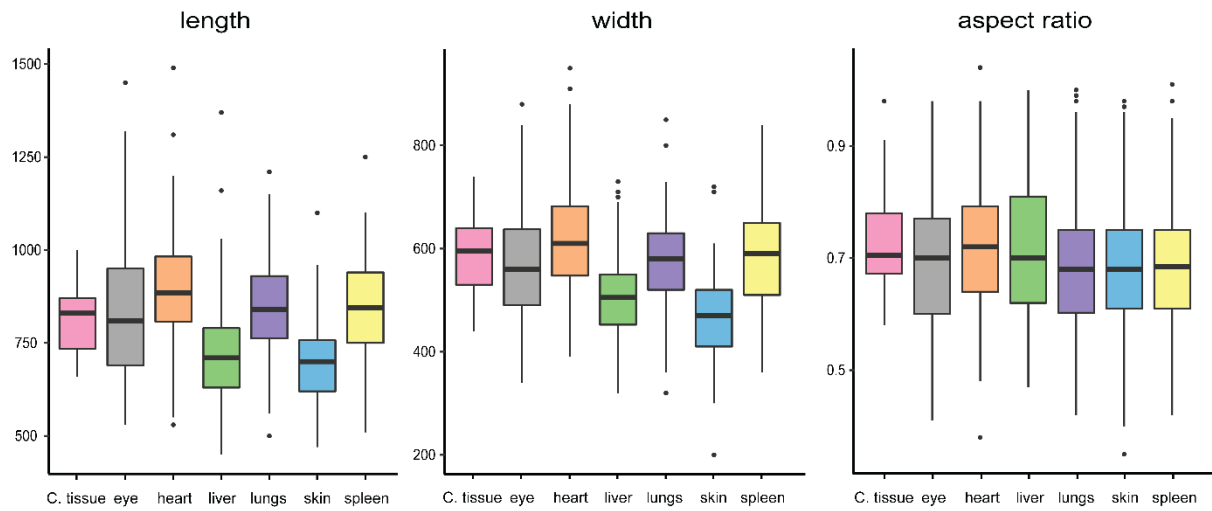


243  
244  
245  
246  
247

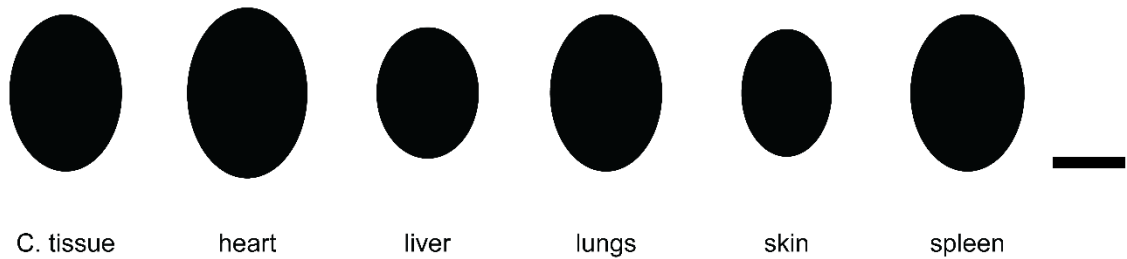
**Fig. S6.** Geometry of melanosomes extracted from extant vertebrate tissues. Diversity of melanosome geometry in amphibians (green), reptiles (black), birds (blue) and mammals (red), with 95% confidence ellipses (*I*).

248

**A** *Xenopus laevis*  
(African clawed frog)



**B**



249

250

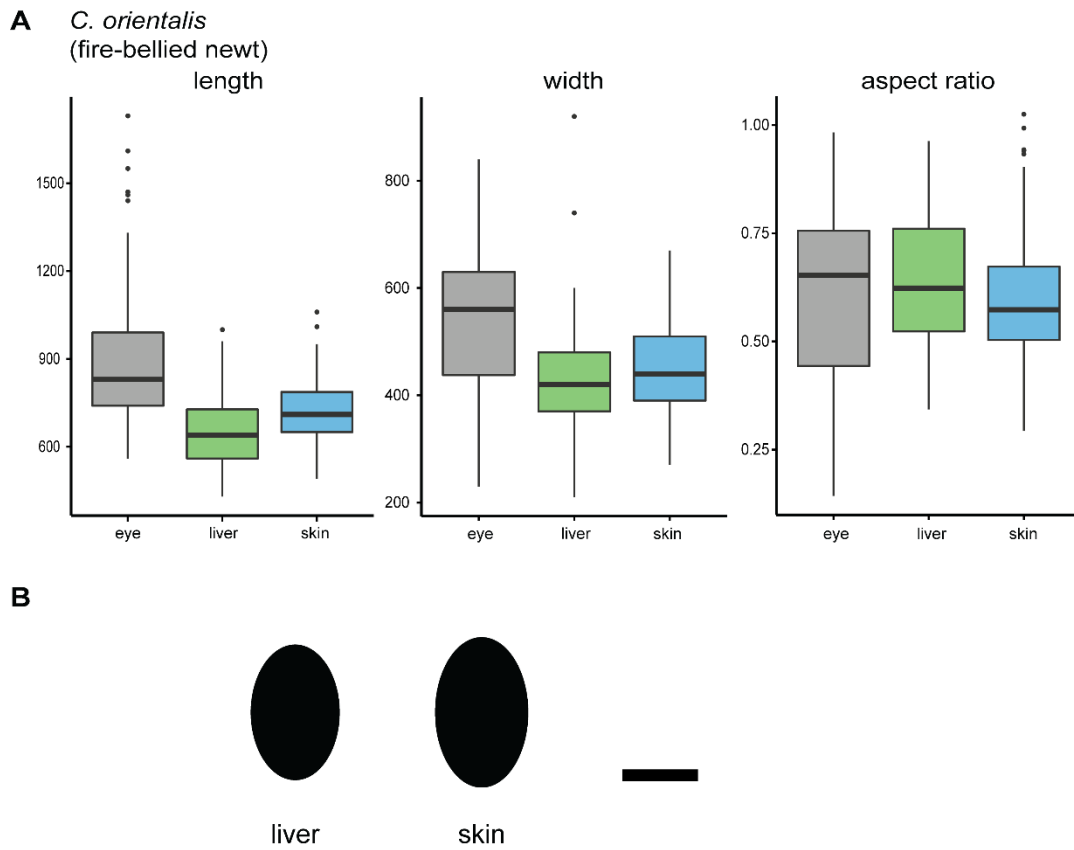
251

252

253

254

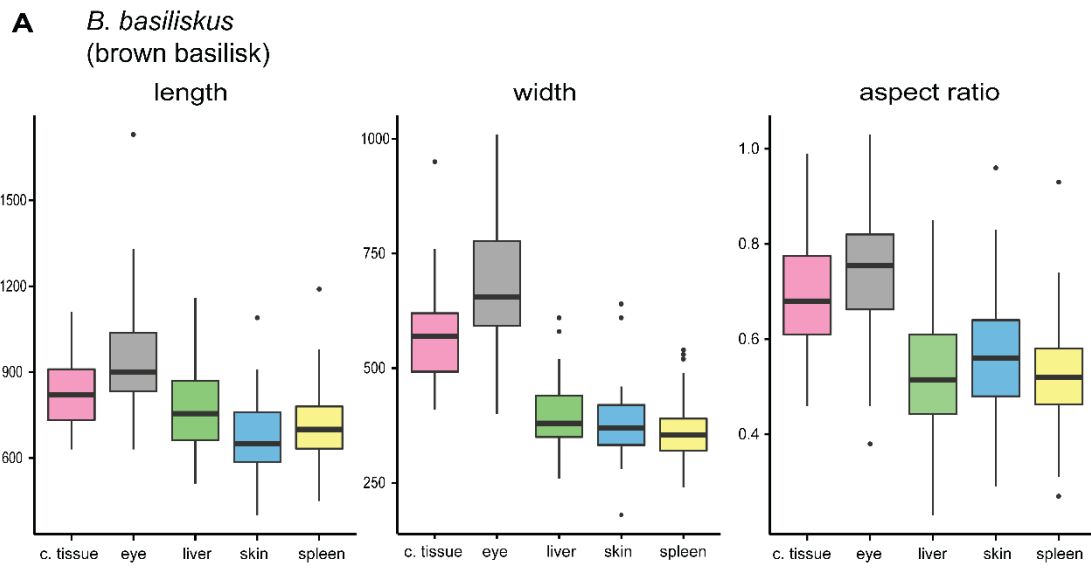
**Fig. S7.** Geometry of melanosomes from tissues in the African clawed frog (*X. laevis*). (A) Box plots of length, width and aspect ratio of melanosomes. (B) Schematic of melanosome morphologies for each tissue analyzed. Scale bar is 0.5  $\mu\text{m}$ .



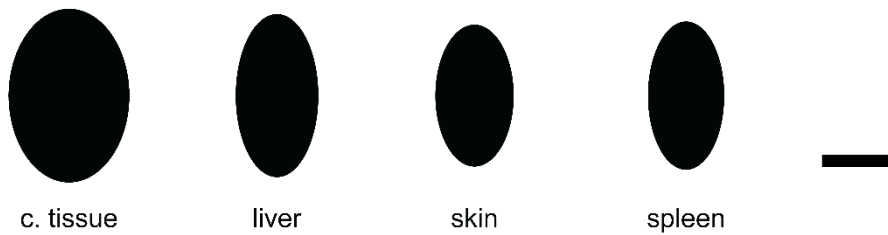
255

256 **Fig. S8.** Geometry of melanosomes from tissues in the fire-bellied newt (*C. orientalis*). (A)  
 257 Box plots of length, width and aspect ratio of melanosomes. (B) Schematic of melanosome  
 258 morphologies for each tissue analyzed. Scale bar is 0.5  $\mu\text{m}$ .

259



**B**



260

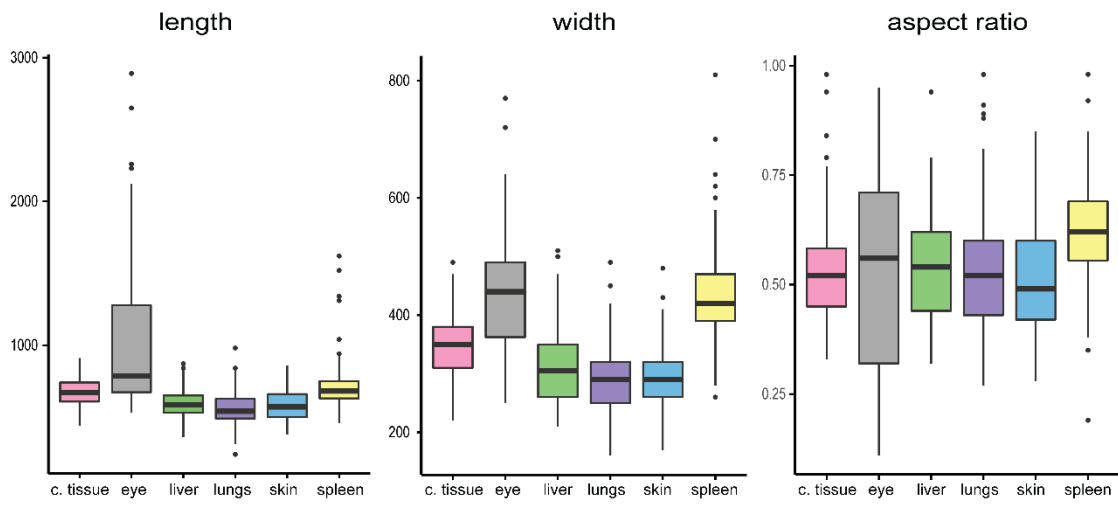
261 **Fig. S9.** Geometry of melanosomes from tissues in the brown basilisk (*B. basiliskus*). (A)  
 262 Box plots of length, width and aspect ratio of melanosomes. (B) Schematic of melanosome  
 263 morphologies for each tissue analyzed. Scale bar is 0.5  $\mu\text{m}$ .

264

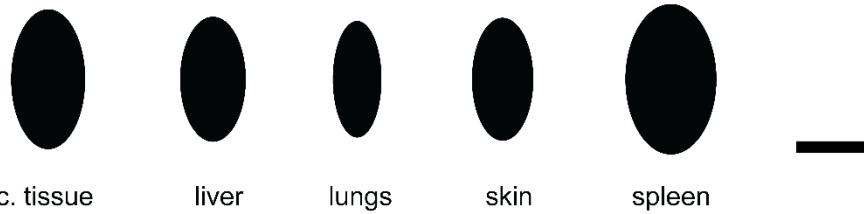
265



**A** *C. similis*  
(black iguana)



**B**

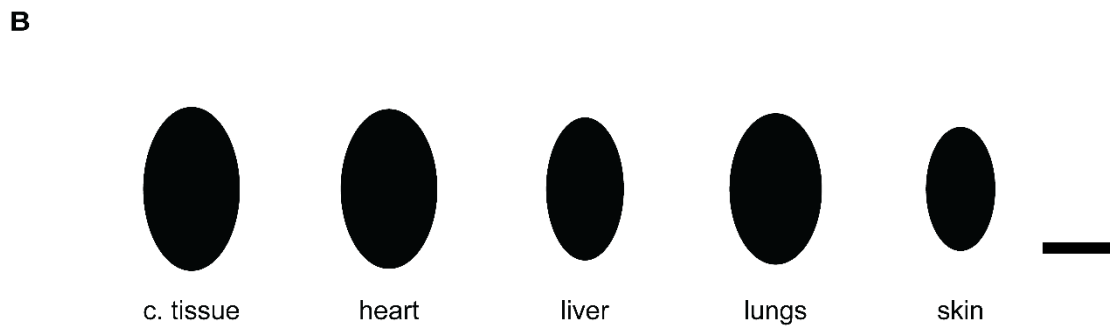
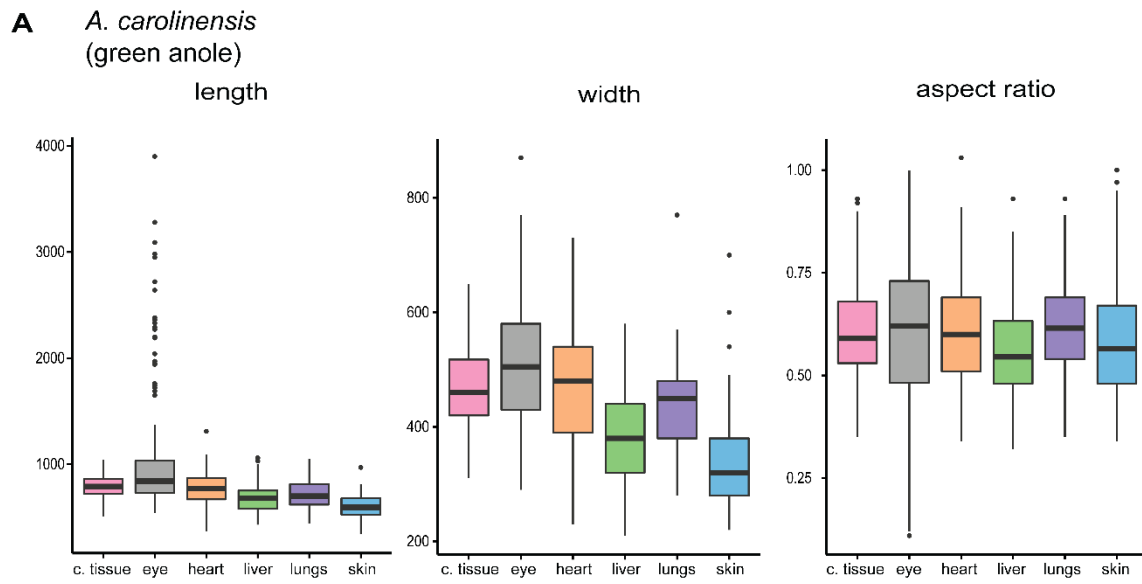


266

267 **Fig. S10.** Geometry of melanosomes from tissues in the black iguana (*C. similis*). (A) Box  
268 plots of length, width and aspect ratio of melanosomes. (B) Schematic of melanosome  
269 morphologies for each tissue analyzed. Scale bar is 0.5  $\mu\text{m}$ .

270

271



272

273

274

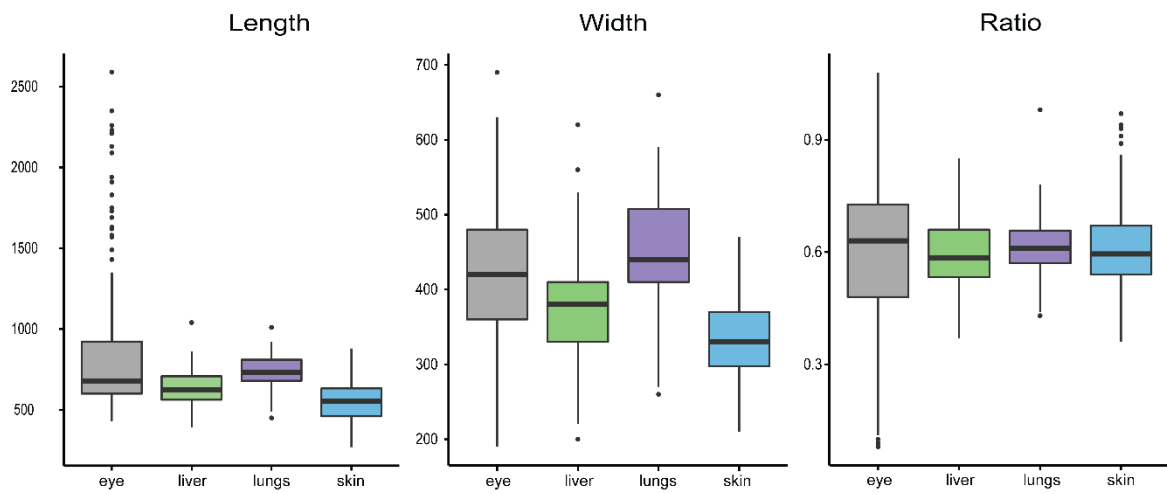
275

276

277

**Fig. S11.** Geometry of melanosomes from tissues in the green anole (*A. carolinensis*). (A) Box plots of length, width and aspect ratio of melanosomes. (B) Schematic of melanosome morphologies for each tissue analyzed. Scale bar is 0.5  $\mu\text{m}$ .

**A** *E. macularius*  
(leopard gecko)



**B**



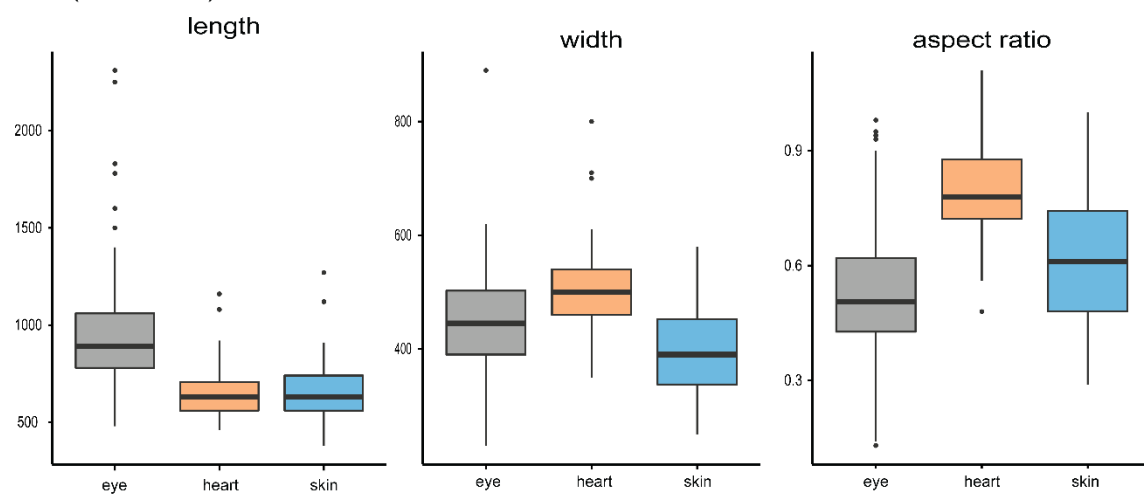
278

279 **Fig. S12.** Geometry of melanosomes from tissues in the leopard gecko (*E. macularius*). (A)  
280 Box plots of length, width and aspect ratio of melanosomes. (B) Schematic of melanosome  
281 morphologies for each tissue analyzed. Scale bar is 0.5  $\mu\text{m}$ .

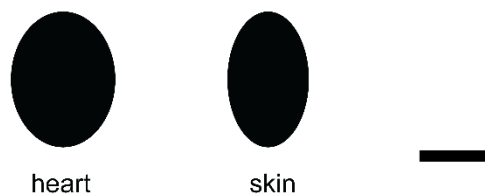
282

283

**A** *T. guttata*  
(zebra finch)



**B**

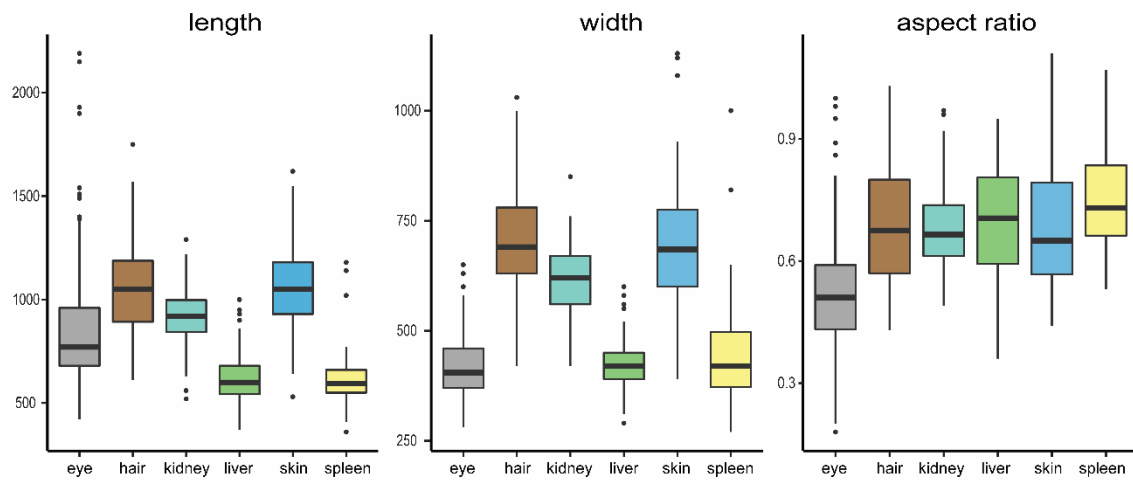


284

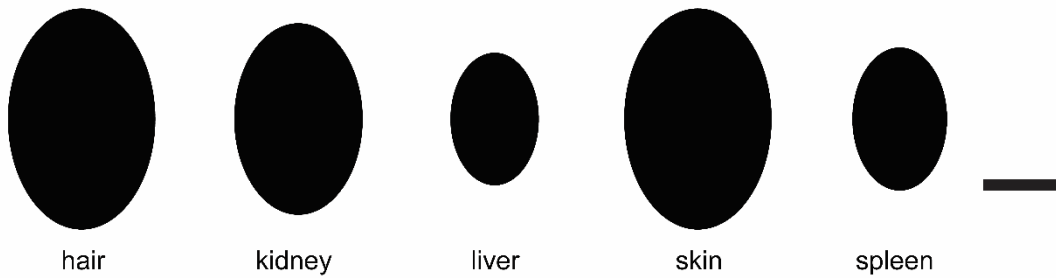
285 **Fig. S13.** Geometry of melanosomes from tissues in the zebra finch (*T. guttata*). (A) Box  
286 plots of length, width and aspect ratio of melanosomes. (B) Schematic of melanosome  
287 morphologies for each tissue analyzed. Scale bar is 0.5  $\mu\text{m}$ .

288

**A** *M. musculus*  
(brown mouse)



**B**

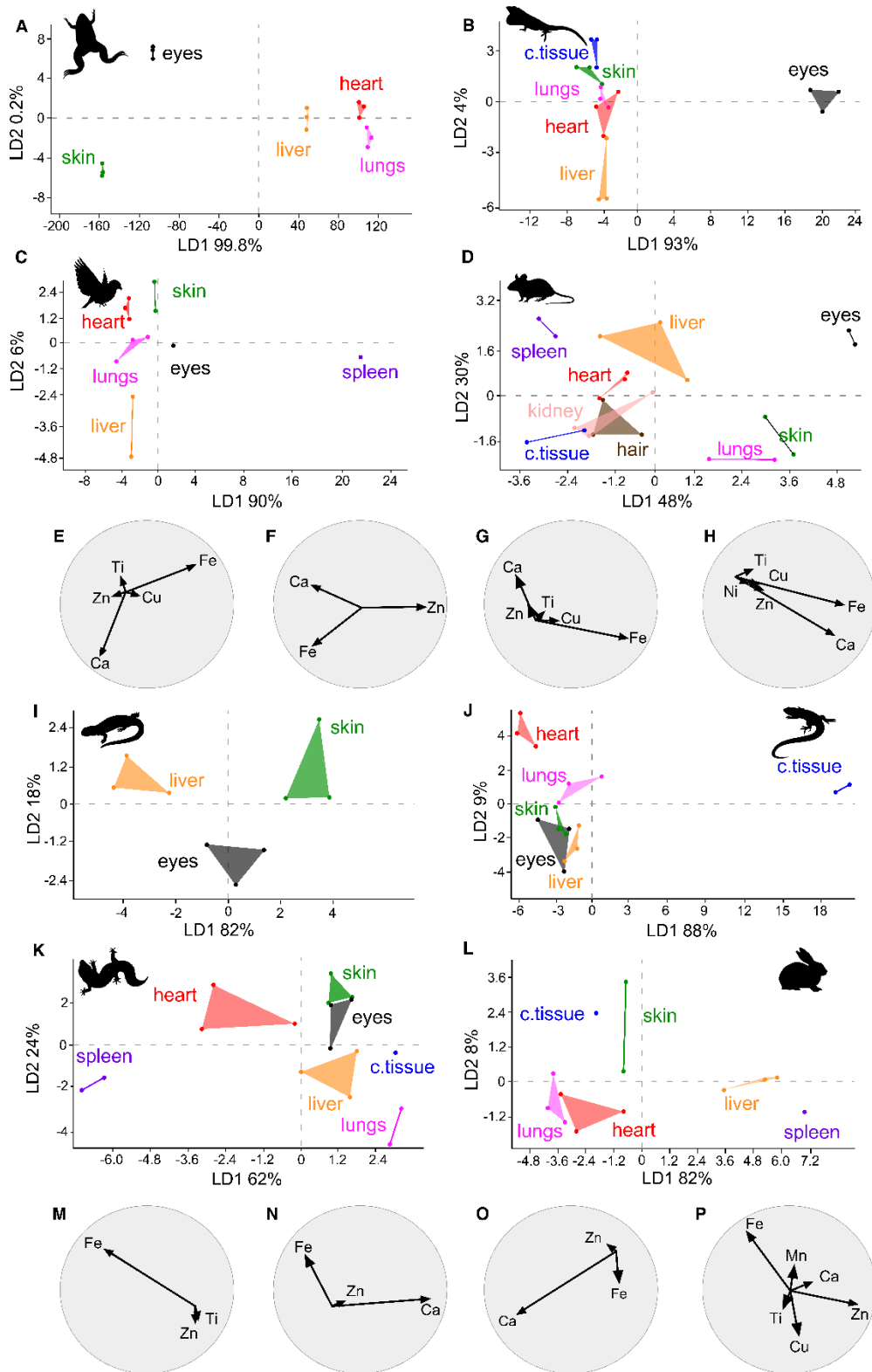


289

290 **Fig. S14.** Geometry of melanosomes from tissues in the brown mouse (*M. musculus*). (A)  
 291 Box plots of length, width and aspect ratio of melanosomes. (B) Schematic of melanosome  
 292 morphologies for each tissue analyzed. Scale bar is 0.5  $\mu\text{m}$ .

293

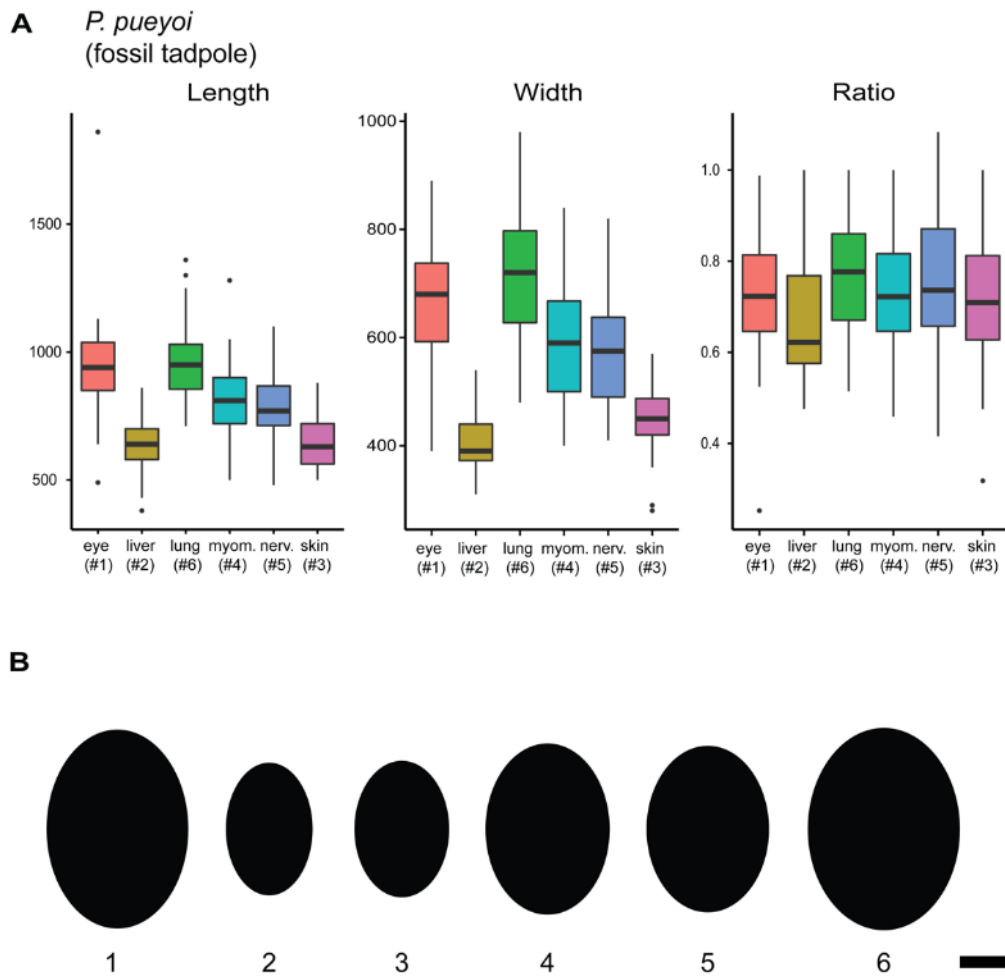
294



295

296 **Fig. S15.** Linear Discriminant Analysis (LDA) of the metal chemistry of melanosomes from  
 297 extant taxa. LDA plots in (A–D, I–L) relate to biplots in (E–H, M–P), respectively. *X. laevis*  
 298 (African clawed frog) (A, E). *A. carolinensis* (green anole) (B, F). *T. guttata* (zebra finch) (C,  
 299 G). *M. musculus* (brown mouse) (D, H). *C. orientalis* (fire-bellied newt) (I, M). *C. similis*  
 300 (black iguana) (J, N). *E. macularius* (leopard gecko) (K, O). *O. cuniculus* (European rabbit)  
 301 (L, P). C. tissue, connective tissue.  
 302



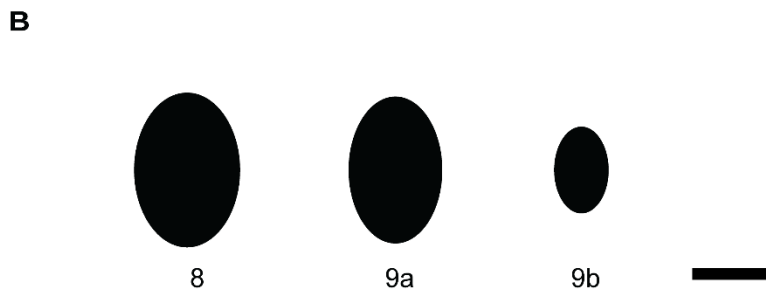
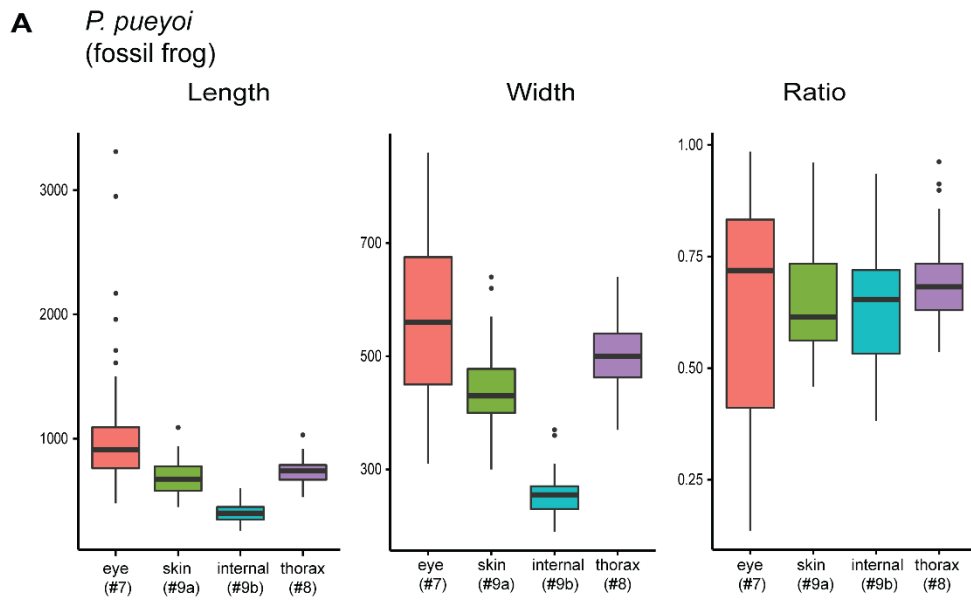


303

304 **Fig. S16.** Geometry of melanosomes preserved in soft tissues of NHML-4999 (*P. pueyoi*).  
 305 (A) Box plots of length, width and aspect ratio of fossil melanosomes. (B) Schematic of  
 306 melanosome morphologies for each soft tissue analyzed. Numbers on the X axis represent  
 307 sampling points in Fig. 2C. myom.: myomeres; nerv.: nerve cord. Scale bar is 0.5  $\mu\text{m}$ .

308

309



310

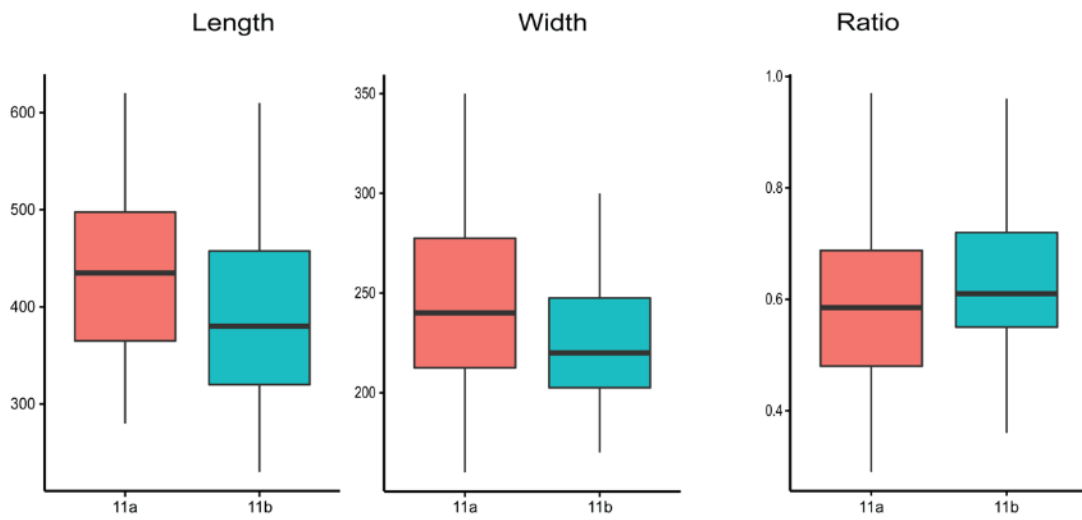
311 **Fig. S17.** Geometry of melanosomes preserved in soft tissues of NHML-4982 (*P. pueyoi*).  
 312 (A) Box plots of length, width and aspect ratio of fossil melanosomes. (B) Schematic of  
 313 melanosome morphologies for each soft tissue analyzed. Numbers on the X axis represent  
 314 sampling points in Fig. 3A. Scale bar is 0.5  $\mu\text{m}$ .

315

316

317

**A** Reptile indet.

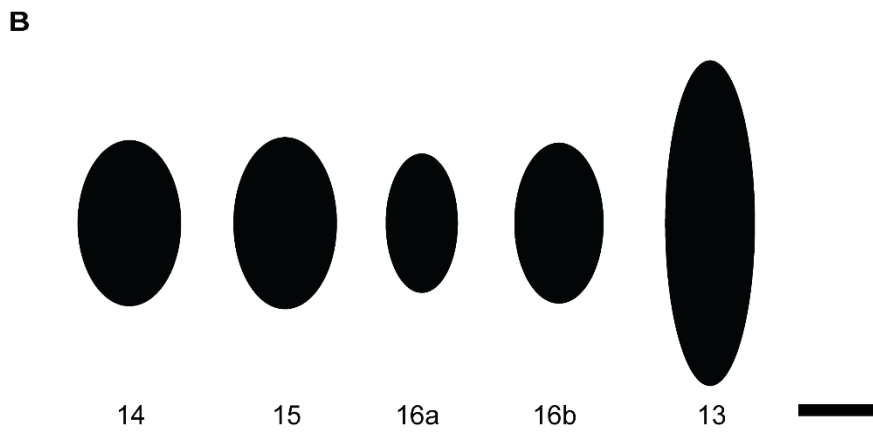
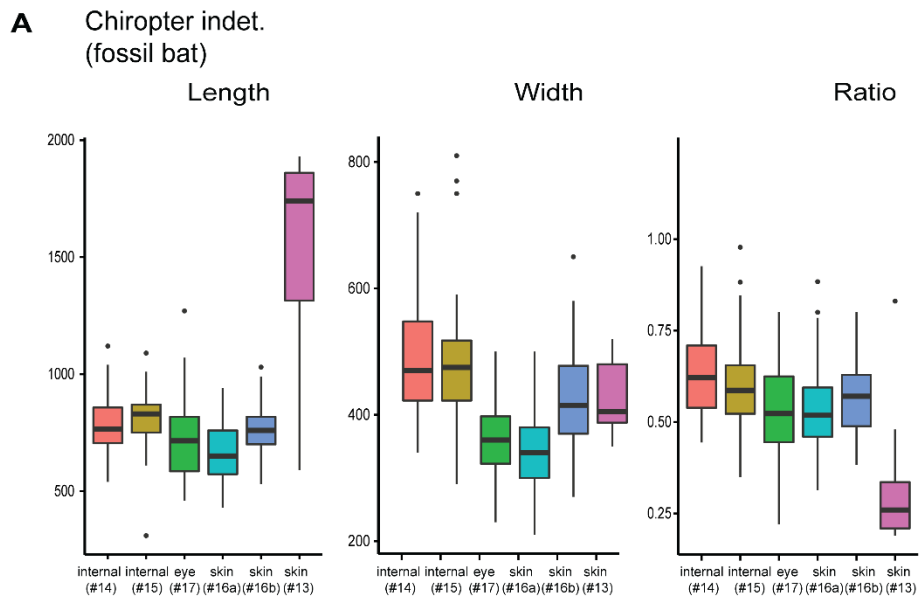


**B**



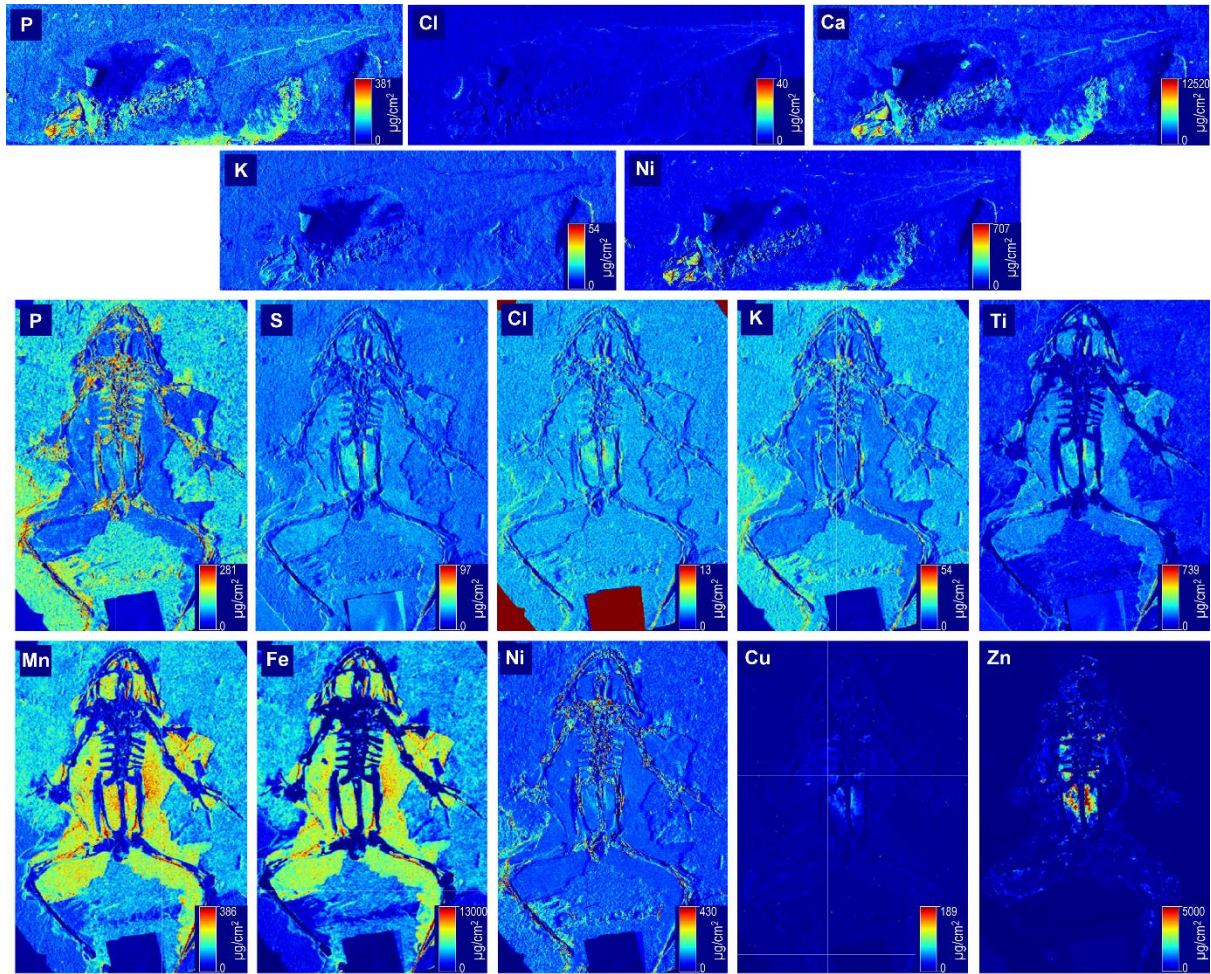
318  
319  
320  
321  
322  
323

**Fig. S18.** Geometry of melanosomes preserved in soft tissues from NHMD-Me9018 (Reptilia indet.). (A) Box plots of length, width and aspect ratio of fossil melanosomes. (B) Schematic of melanosome morphologies for each soft tissue analyzed. Numbers on the X-axis represent sampling points in Fig. 5E and I. Scale bar is 0.5  $\mu\text{m}$ .



324 **Fig. S19.** Geometry of melanosomes preserved in soft tissues of HNMD-Me7069b  
 325 (Chiroptera indet.). (A) Box plots of length, width and aspect ratio of fossil melanosomes. (B)  
 326 Schematic of melanosome morphologies for each soft tissue analyzed. Numbers on the X  
 327 axis represent sampling points in Fig. 3C. Scale bar is 0.5  $\mu$ m.  
 328

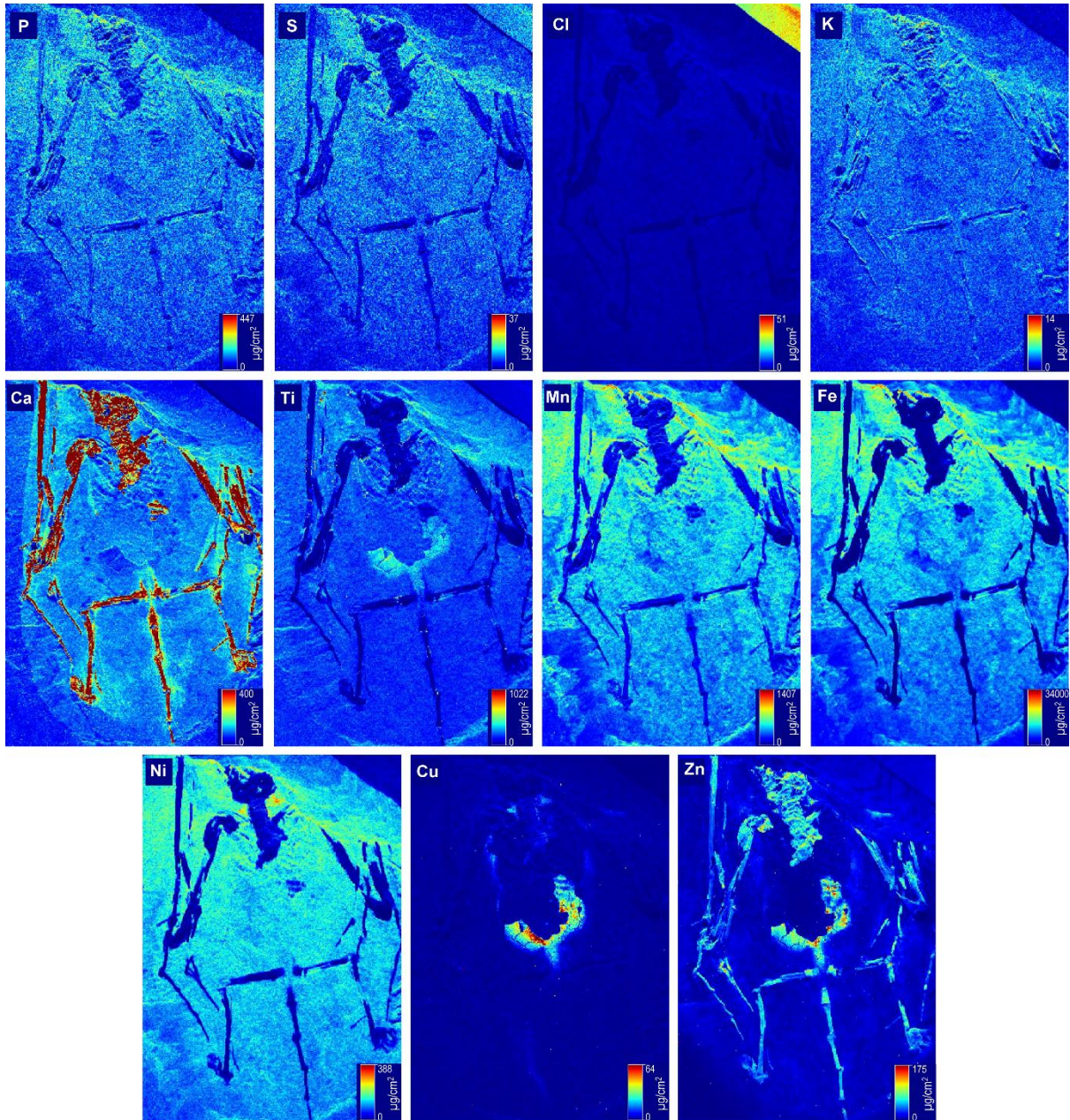
329  
 330



331

332 **Fig. S20.** SRS-XRF maps of NHML-4999 (*Pelophylax pueyoi*, tadpole) and NHML-4982  
 333 (*Pelophylax pueyoi*, frog) from Libros. In NHML-4982, Ca is not partitioned into specific  
 334 regions of the soft tissues and thus maps are not shown here (but see Fig. 3 for tricolor plot  
 335 including data for Ca).  
 336



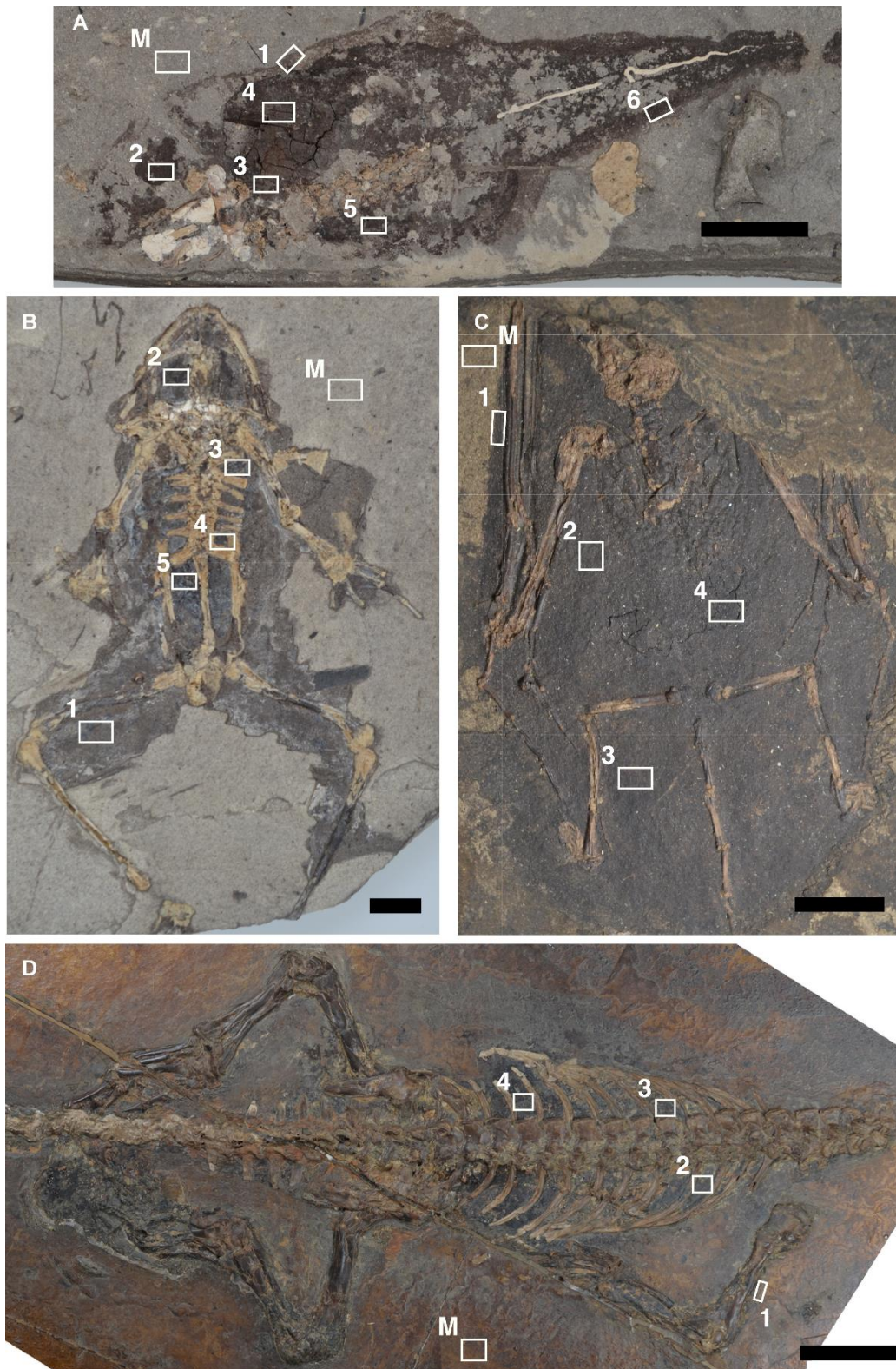


337

338 **Fig. S21.** SRS-XRF maps of a fossil bat (HMLD-Me7069b (Chiroptera indet.)) from Messel.  
 339 Local loss of soft tissue layer and ribs in the torso, revealing underlying sediment, is visible  
 340 in maps for Ti, Cu and Zn.

341

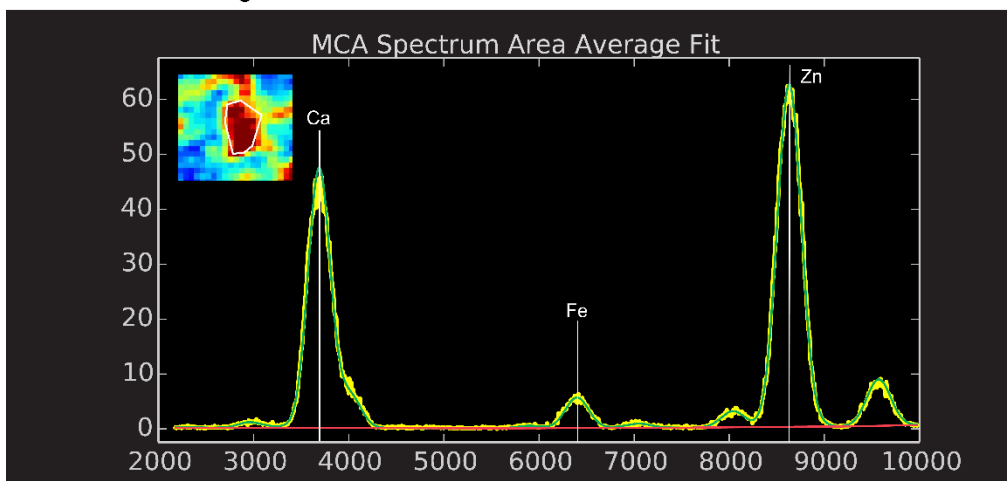




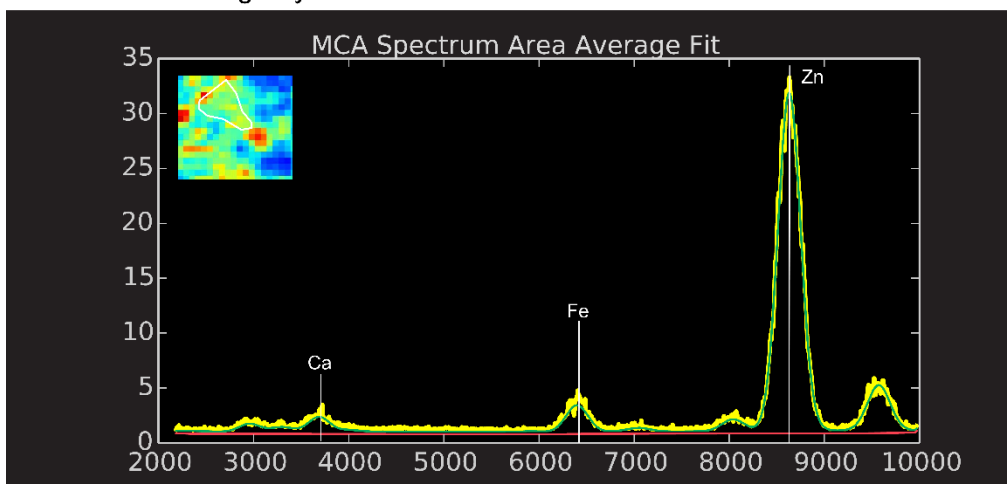
342  
 343  
 344  
 345  
 346  
 347

**Fig. S22.** Regions of interest (ROIs, white rectangles) analyzed using LDA (data shown in Fig. 6). (A) NHML-4999 (*P. pueyoi*, tadpole). (B) NHML-4982 (*P. pueyoi*). (C) HMLD-Me7069b (Chiroptera indet.). (D) HMLD-Me9018 (Reptilia indet.). ‘M’ denotes sediment in A–C and resin in D. Scale bars: 10 mm.

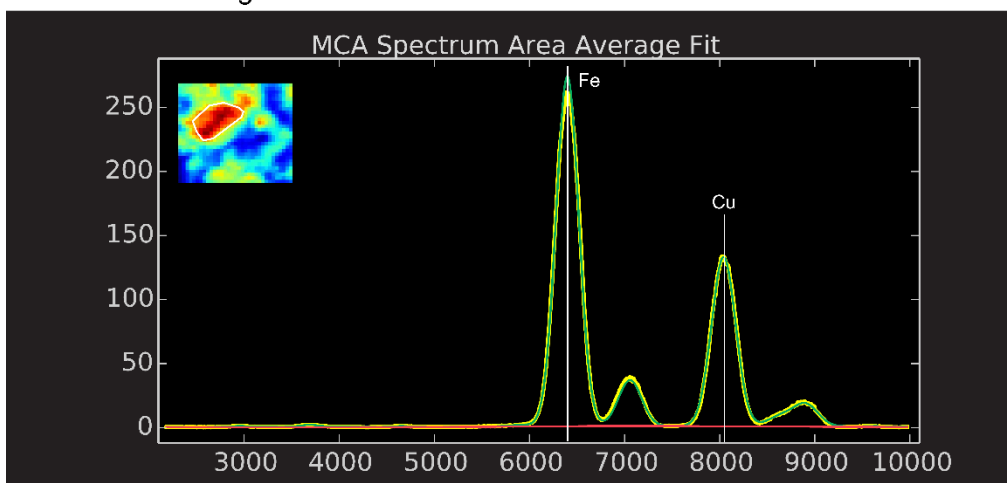
African Clawed frog - skin



African Clawed frog - eye



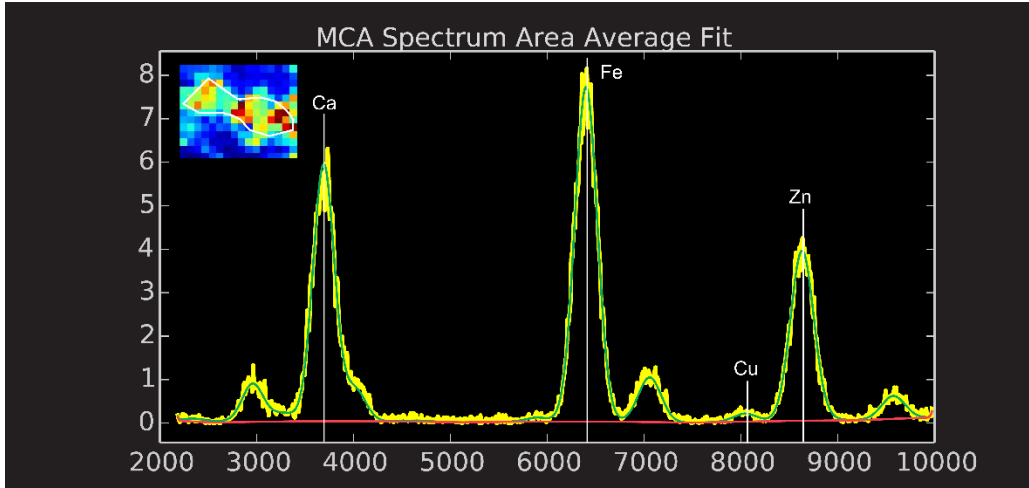
African Clawed frog - liver



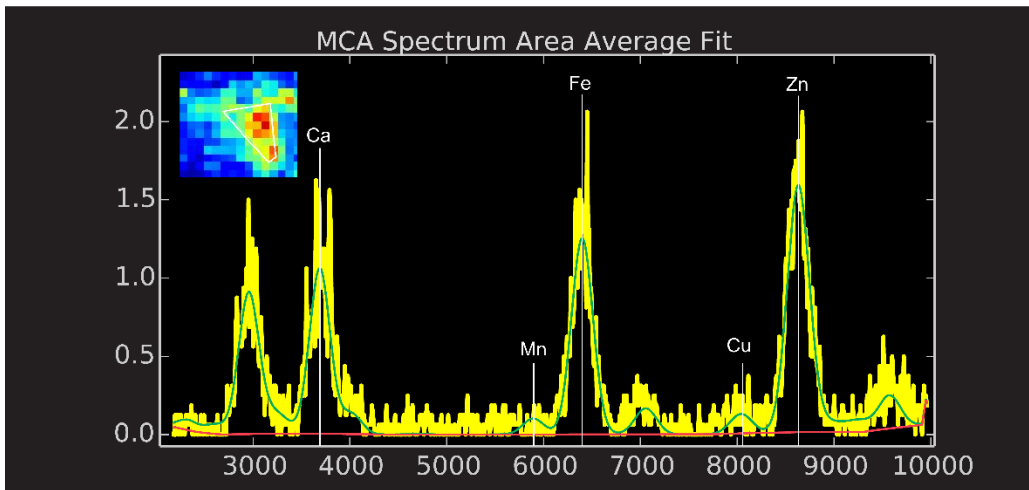
348  
349  
350  
351  
352  
353

**Fig. S23.** MCA spectra of melanosomes samples from the skin, eye and liver of the African clawed frog (*X. laevis*). X-axis represent X-ray emission energy in eV; Y-axis represent counts.

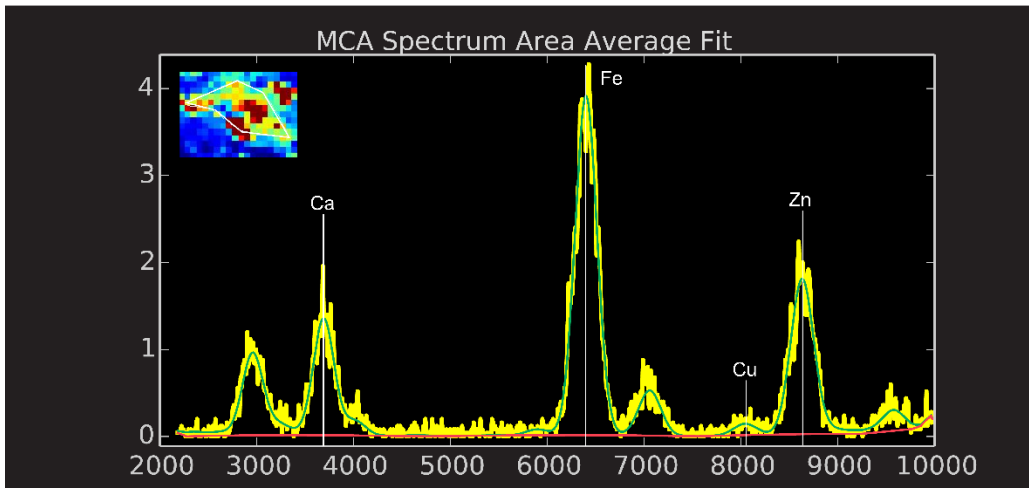
Black iguana - skin



Black iguana - eye



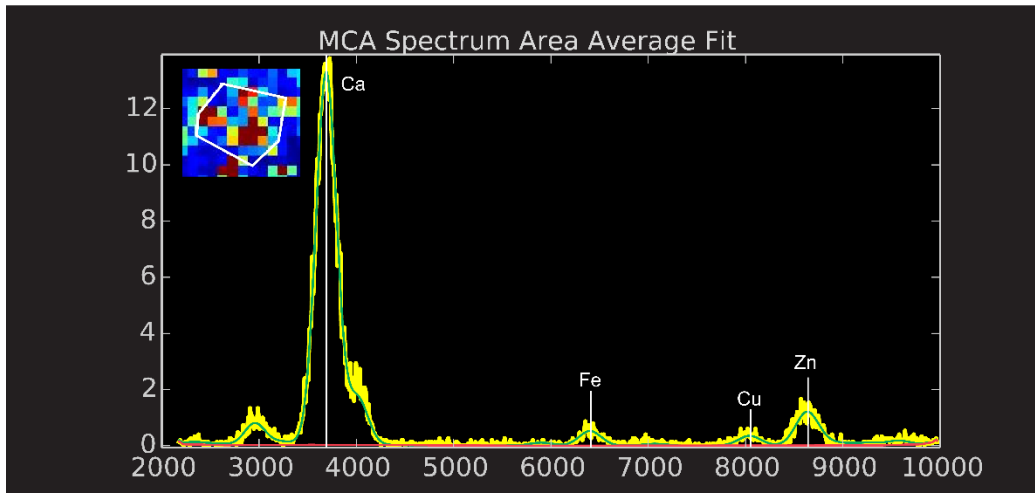
Black iguana - liver



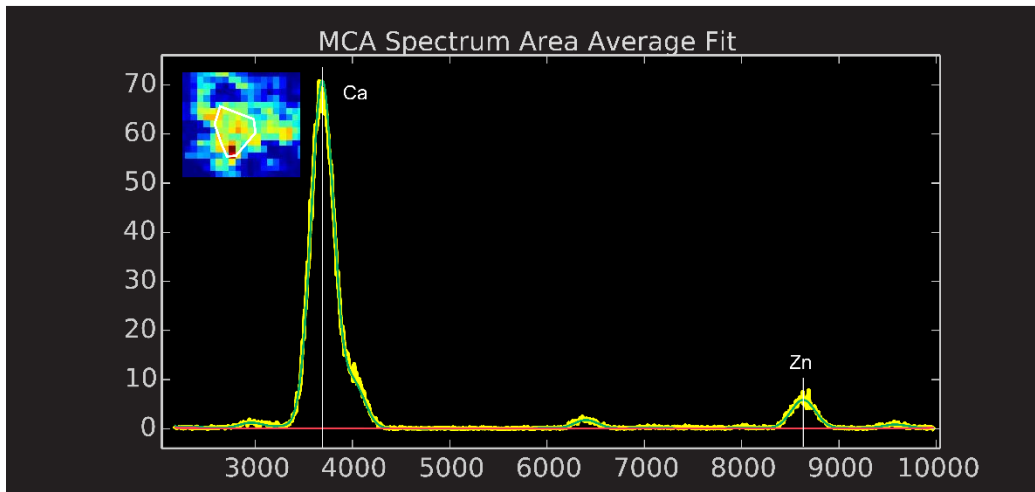
354  
355  
356  
357

**Fig. S24.** MCA spectra of melanosomes samples from the skin, eye and liver of the black iguana (*C. similis*). X-axis represent X-ray emission energy in eV; Y-axis represent counts.

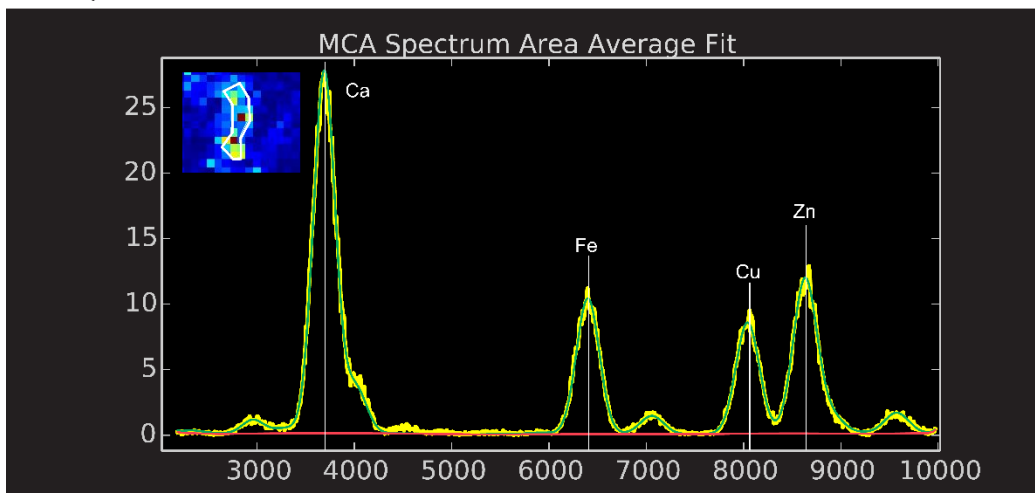
Java sparrow - skin



Java sparrow - eye



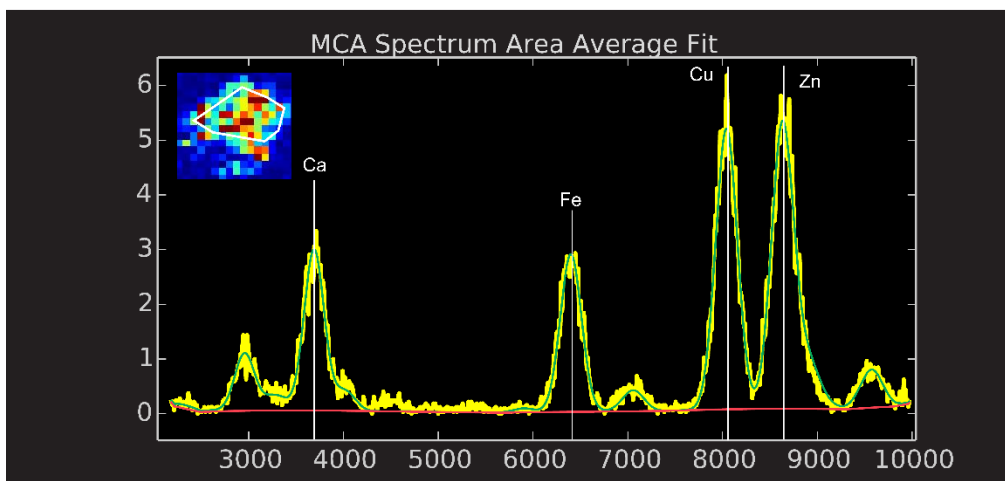
Java sparrow - liver



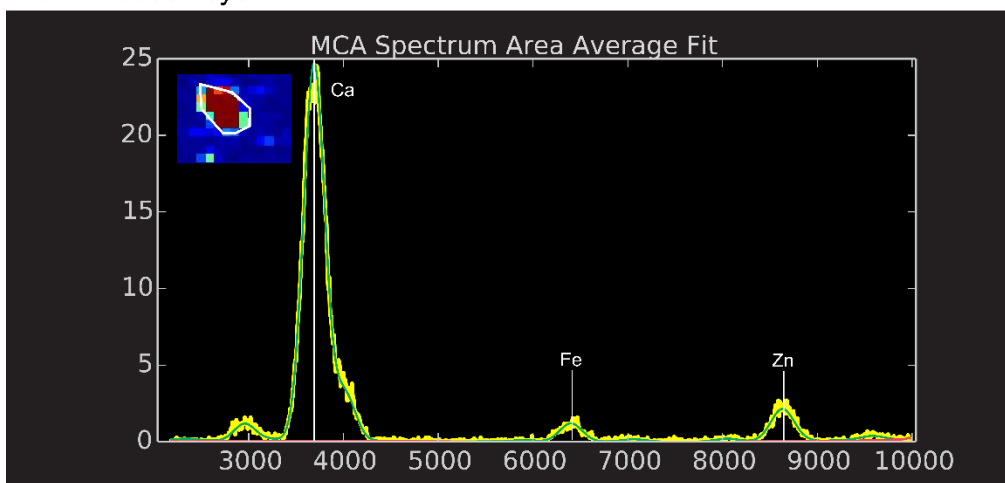
358  
359  
360  
361  
362  
363

**Fig. S25.** MCA spectra of melanosomes samples from the skin, eye and liver of the Java sparrow (*L. orizyvara*). X-axis represent X-ray emission energy in eV; Y-axis represent counts.

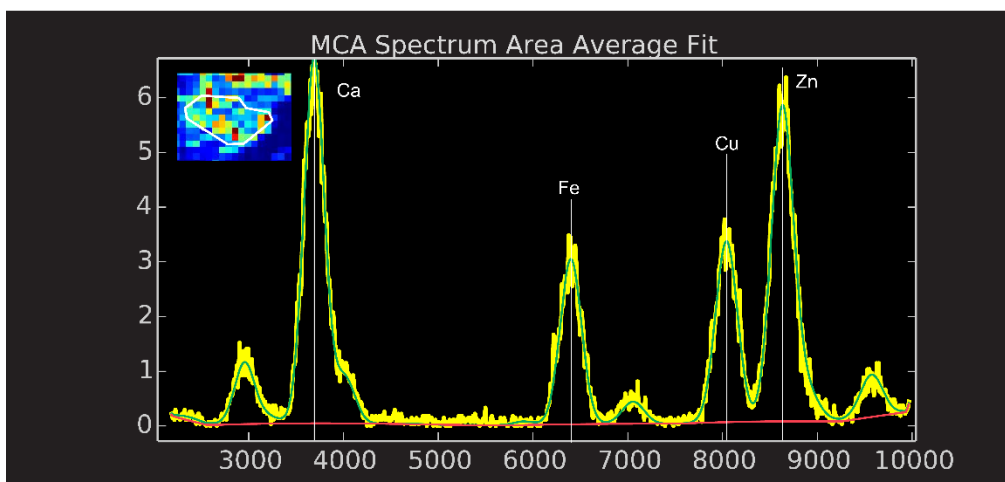
Brown mouse - skin



Brown mouse - eye



Brown mouse - liver

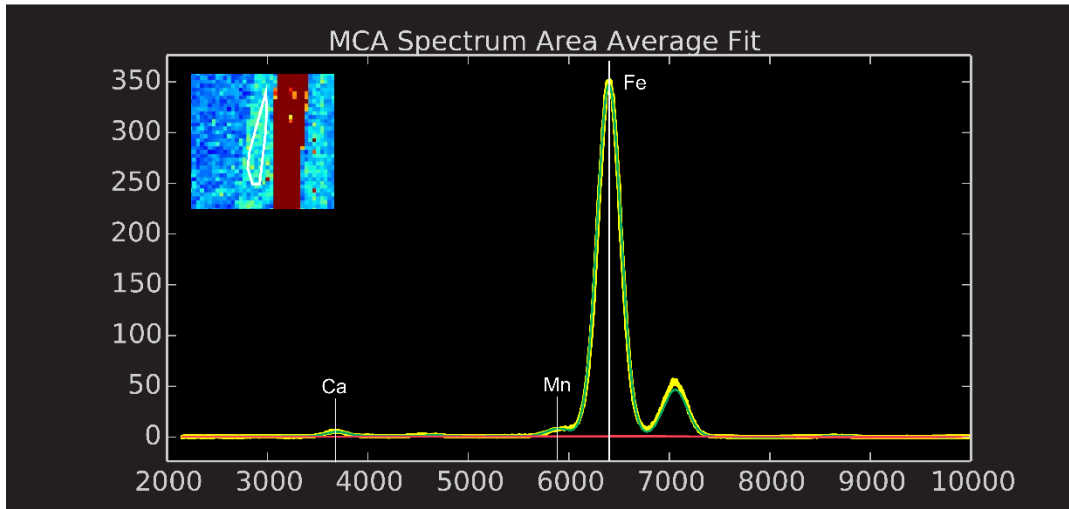


364  
365  
366  
367  
368  
369

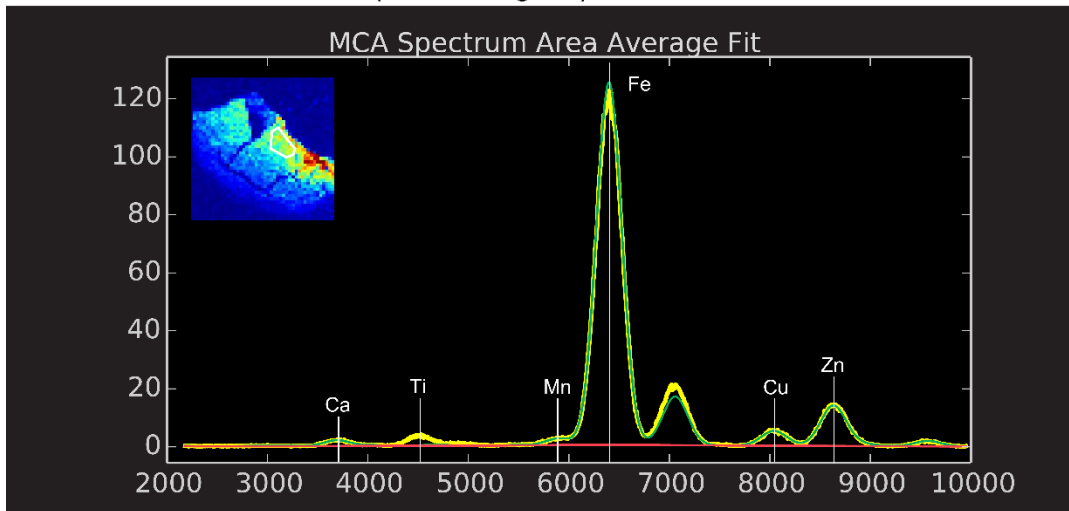
**Fig. S26.** MCA spectra of melanosomes samples from the skin, eye and liver of the brown mouse (*M. musculus*). X-axis represent X-ray emission energy in eV; Y-axis represent counts.



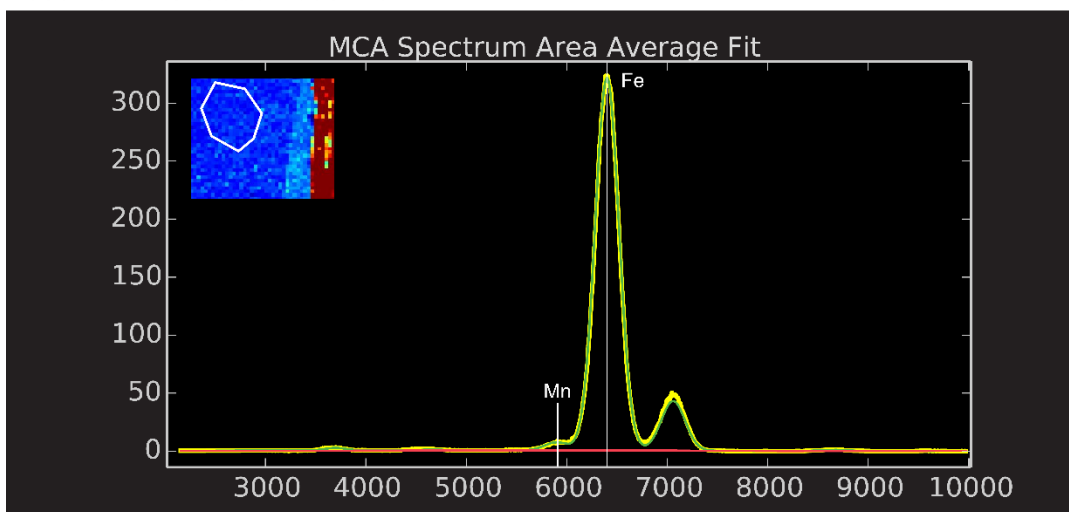
Fossil bat Me7069b - ROI1 (skin)



Fossil bat Me7069b - ROI4 (internal organs)



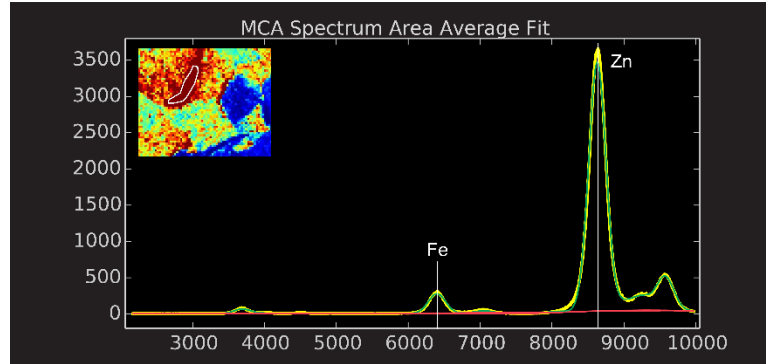
Fossil bat Me7069b - sediment



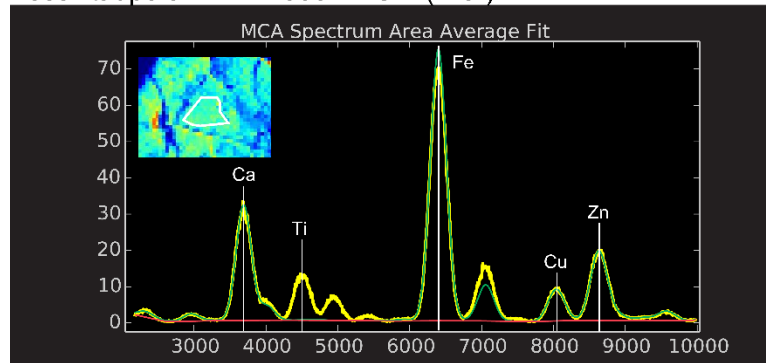
370  
371  
372  
373  
374

**Fig. S27.** MCA spectra of ROIs and sediment of the fossil bat Me7069b (Chiroptera indet.). X-axis represent X-Ray emission energy in eV; Y-axis represent counts.

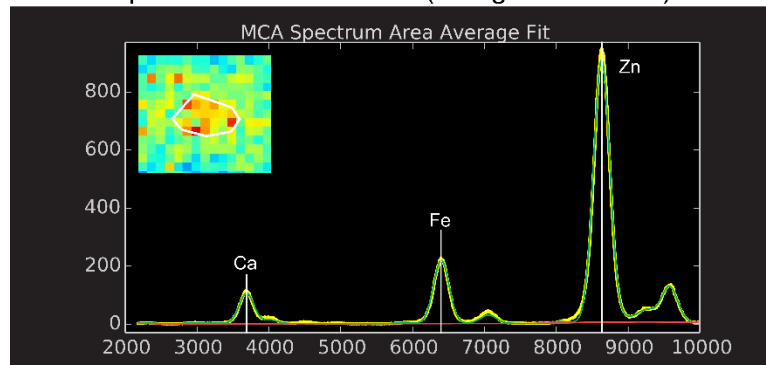
Fossil tadpole NHML4999 - ROI2 (eye spot)



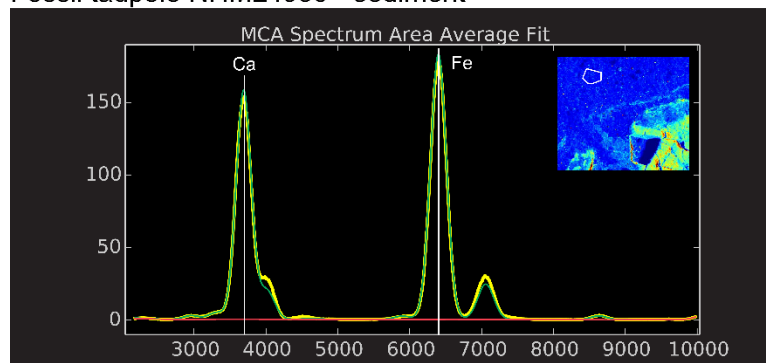
Fossil tadpole NHML4999 - ROI4 (liver)



Fossil tadpole NHML4999 - ROI6 (collagenous fascia)

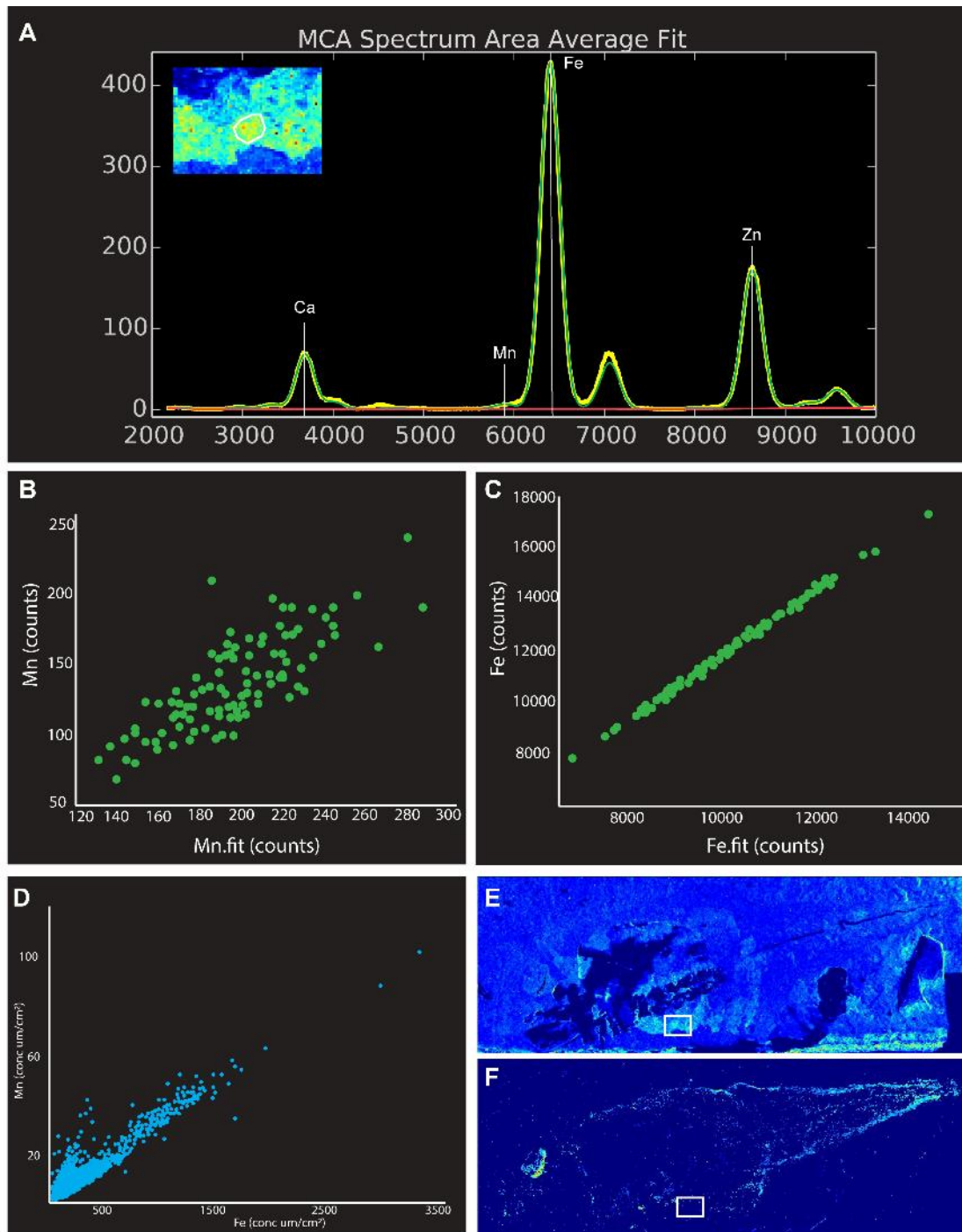


Fossil tadpole NHML4999 - sediment



375  
376  
377  
378

**Fig. S28.** MCA spectra of ROIs and sediment of the fossil tadpole NHML4999 (*P. pueyoi*). X-axis represent X-Ray emission energy in eV; Y-axis represent counts.



379  
 380  
 381  
 382  
 383  
 384  
 385  
 386  
 387

**Fig. S29.** Analysis of ROI5 of the fossil tadpole NHML4999 (*P. pueyoi*). MCA spectrum (A); correlation plots for Mn and Fe after peak fitting (B and C): similar trends suggest that Mn (B) is present but at very low counts in comparison with a clear signal for Fe (C). Correlation plot (D) of concentrations ( $\mu\text{m}/\text{cm}^2$ ) of Mn and Fe. Maps produced using the correlation plot data for Fe (E) and Mn (F) show that Mn is very low/absent in ROI5 (white rectangle). X-axis in A–D represents X-ray emission energy in eV; Y-axis represents counts (A).



388 **Dataset S1. Summary of materials and methods used in this study.**  
389 AHPO and HI, alkaline hydrogen peroxide oxidation and acid hydrolysis; SRS-XRF,  
390 synchrotron rapid scanning-X-ray fluorescence. yes: sample was available for the analysis;  
391 no: sample was not available for analysis; not attempted: sample was not available for  
392 analysis.  
393

394 **Dataset S2. List of fossil vertebrates analyzed.**  
395

396 **Dataset S3. Alkaline hydrogen peroxide oxidation (AHPO) analysis of fossil and extant**  
397 **samples.** PTCA, pyrrole-2,3,5-tricarboxylic acid (PTCA); PTeCA, pyrrole-2,3,4,5-  
398 tetracarboxylic acid; 4-AHP, 4-amino-3-hydroxyphenylalanine.  
399

400 **Dataset S4. Percentage area of tissue occupied by melanin in histological sections.**  
401 st. dev., standard deviation.  
402

403 **Dataset S5. ANOVA and post-hoc Tukey test results using histology data on the**  
404 **abundance of melanosomes in different tissues (as per Datasets S8 and S9).** Bold font  
405 denotes statistically significant p-values.  
406

407 **Dataset S6. Geometry of melanosomes in extracts from tissues of extant vertebrates.**  
408 Mean and standard deviation (st. dev.; both in  $\mu\text{m}$ ) of length, width and aspect ratio.  
409

410 **Dataset S7. ANOVA of geometry for melanosomes from tissue extracts.**  
411 Bold font indicates statistically significant p-values. Except where indicated by (\*), all test  
412 results are ANOVA F-values. Asterisk (\*) indicates use of Kruskal-Wallis test for non-  
413 normally distributed data.  
414

415 **Dataset S8. Tukey and Mann-Whitney post-hoc test results following ANOVA of**  
416 **melanosome geometry data from extant vertebrates.** Bold font indicates statistically  
417 significant p-values.\* indicates use of Mann-Whitney test for non-normally distributed data.  
418

419 **Dataset S9. Mean and standard deviation (SD; both in  $\mu\text{g}/\text{cm}^2$ ) of concentration data for**  
420 **all elements analyzed.** Npix: number of pixels per ROI.  
421

422 **Dataset S10. Geometry of fossil melanosomes.** Mean and standard deviation of length,  
423 width and aspect ratio. Each ROI (region of interest) corresponds to a specific sample point  
424 (shown in Fig. 4). Empty cells refer to samples where melanosomes were not observed with  
425 SEM. St. dev., standard deviation.  
426

427 **Dataset S11. ANOVA on fossil melanosome geometry.** Bold font denotes statistically  
428 significant p-values.  
429

430 **Dataset S12. Tukey and Mann-Whitney (\*) post-hoc tests on fossil melanosome**  
431 **geometry data.** Bold font denotes statistically significant p-values.  
432

433 **Dataset S13. Raw data on elemental chemistry of fossil vertebrate melanosomes.** Each  
434 line corresponds to one pixel ( $25 \times 25 \mu\text{m}$ ) of each elemental map. Regions of interest (ROIs)  
435 are numbered as in Fig. 6 and Fig. S22.  
436

437 **Dataset S14. Loadings (LDA) of fossil melanosome trace element chemistry.**

438

439 **Dataset S15. ANOVA test on fossil melanosome trace element chemistry.** Bold font  
440 denotes statistically significant p-values. All samples are highly significant.

441

442 **Dataset S16. Tukey post-hoc test on fossil melanosome trace element chemistry.** Bold  
443 font denotes statistically significant p-values.

444

445  
446  
447  
448  
449  
450  
451  
452  
453  
454  
455  
456  
457  
458  
459  
460  
461  
462  
463  
464  
465  
466  
467  
468  
469

## References

1. Liu Y, et al. (2003) Comparison of the structural and physical properties of human hair eumelanin following enzymatic or acid / base extraction. *Pigment Cell Res.* 16, 355–365.
2. Liu Y, et al. (2007) Comparison of structural and chemical properties of black and red human hair melanosomes. *Photochem Photobiol* 81, 135–144.
3. Colleary C, et al. (2015) Chemical, experimental, and morphological evidence for diagenetically altered melanin in exceptionally preserved fossils. *Proc. Natl. Acad. Sci.* 112, 12592–12597.
4. Hong L, Simon JD (2007) Current understanding of the binding sites, capacity, affinity, and biological significance of metals in melanin. *J. Phys. Chem. B.* 111, 7938–7947.
5. Limburg KE, Huang R, Bilderback D (2007) Fish otolith trace element maps: new approaches with synchrotron microbeam x-ray fluorescence. *X-Ray Spectrom.* 36, 336–342.
6. McNamara, ME et al. (2009) Soft-tissue preservation in Miocene frogs from Libros, Spain: insights into the genesis of decay microenvironments. *Palaios* 24, 104–117.
7. Lenz, OK, Wilde, V, Mertz, DF & Riegel, W (2015) New palynology-based astronomical and revised  $^{40}\text{Ar}/^{39}\text{Ar}$  ages for the Eocene maar lake of Messel (Germany). *Int. J. Earth Sci.* 104, 873–889.
8. Harms, FJ (2002) Steine erzählen Geschichte: Ursache für die Entstehung des Messel-Sees gefunden. *Natur und Museum.* 132, 1–4.